WIRELESS THIN-FILM MICROWAVE RESONATORS FOR SENSING AND MARKING

A DISSERTATION SUBMITTED TO

THE GRADUATE SCHOOL OF ENGINEERING AND SCIENCE

OF BILKENT UNIVERSITY

IN PARTIAL FULFILLMENT OF THE REQUIREMENTS FOR

THE DEGREE OF

DOCTOR OF PHILOSOPHY

IN

ELECTRICAL AND ELECTRONICS ENGINEERING

By

Akbar Alipour

May 2017

WIRELESS THIN-FILM MICROWAVE RESONATORS FOR SENSING AND MARKING

By Akbar Alipour

May 2017

We certify that we have read this dissertation and that in our opinion it is fully adequate, in scope and in quality, as a dissertation for the degree of Doctor of Philosophy.

Hilmi Volkan Demir (Advisor)

Ergin Atalar

Yeşim Serinağaoğlu Doğrusöz

Tolga Çukur

Hatice Kader Karlı Oğuz

Approved for the Graduate School of Engineering and Science:

Ezhan Karaşan
Director of the Graduate School

ABSTRACT

WIRELESS THIN-FILM MICROWAVE RESONATORS FOR SENSING AND MARKING

Akbar Alipour
Ph.D. in Electrical and Electronics Engineering
Advisor: Hilmi Volkan Demir
May 2017

Rapid progress in wireless microwave technology has attracted increasing interest for high-performance wireless devices. The thin-film microwave technology is now evolving into the mainstream of applications but significant advances are required in resonator architectures and processing for operation in the desired frequency ranges. This dissertation studies the thin-film microwave technology to develop wireless resonators and describes the core elements that give rise to resonators for high performance in wireless sensing and marking. Specific to wireless sensing, we proposed and developed a novel wireless microwave resonator scheme that enables telemetric strain sensing avoiding the need for calibration at different interrogation distances. In this work, we showed that by using both the proposed sensor architecture and wireless measurement method, strain can be successfully extracted independent of the interrogation distance for the first time. The experimental results indicate high sensitivity and linearity for the proposed system. This approach enables mobile wireless sensing with varying interrogation distance. For wireless marking, we investigated an ultra-thin, flexible, passive radio frequency (RF) based resonator compatible with magnetic resonance imaging (MRI) that successfully was tested in clinic. The ultra-thin and flexible architecture of the device offers an effective and safe MR visualization and improves the feasibility and reliability of anatomic marking at various surfaces of the body. Results show that, at low background flip angles, the proposed structure enables precise and rapid visibility with high marker-to-background contrast as well as high signal-to-noise ratio (SNR). Also clinical studies have led to a successful biopsy procedure using marking functionality of our device. In another work related to marking, we proposed a new method to enhance local SNR and resolution without disturbing the B1-field. Here we used our passive RF resonator in the inductively uncoupled mode for endocavity MR imaging. T_1- and T_2-weighted sequences were employed for phantom and in vivo experiments. The obtained images show the feasibility of the proposed technique to improve the SNR and

the resolution in the vicinity of the device. These findings will allow for new possibilities in applications using wireless sensing and marking approaches shown in this thesis.

Keywords: Magnetic resonance imaging, thin-film microwave resonator, inductive coupling, MRI marker, wireless passive resonator, RF excitation, strain sensing.

ÖZET

ALGILAMA VE İŞARETLEME İÇİN KABLOSUZ İNCE-FİLM MİKRODALGA REZONAÖRLER

Akbar Alipour
Elektrik ve Elektronik Mühendisliği, Doktora
Tez Danışmanı: Hilmi Volkan Demir
Mayıs 2017

Kablosuz mikrodalga teknolojisindeki hızlı ilerlemeyle birlikte yüksek performanslı kablosuz cihazlara olan ilgi artmaktadır. Bu alandaki uygulamalarda ince-film mikrodalga teknolojisi kendisine daha çok yer bulmasına rağmen rezonatör mimarisinde ve rezonatörleri istenilen frekans aralıklarında işlemeye yönelik tekniklerde gelişmelere ihtiyaç duyulmaktadır. Bu tez çalışmasında kablosuz rezonatör geliştirmek amacı ile ince-film mikrodalga teknolojisi incelenmiş ve kablosuz algılama ve işaretlemede yüksek performans için gerekli olan çekirdek öğeler tanımlanmıştır. Kablosuz algılamaya özgü olarak, farklı sorgulama uzaklıklarında kalibrasyon ihtiyacını ortadan kaldırarak uzaktan gerinim algılamayı mümkün kılan yeni bir kablosuz mikrodalga rezonatör yapısı önerilmiş ve geliştirilmiştir. Bu çalışmada önerilen sensor mimarisi ve kablosuz ölçüm yöntemi beraber kullanılarak gerilmenin sorgu uzaklığından bağımsız olarak ölçülebileceği ilk kez gösterilmiştir. Deney sonuçları önerilen sistem için yüksek hassasiyet ve doğrusallığı göstermektedir. Bu yaklaşım, çeşitli sorgulama mesafelerinde mobil kablosuz algılamayı mümkün kılmaktadır.

Bunun yanı sıra ince-film teknolojisi kullanılarak manyetik rezonans görüntüleme (MRG) sırasında işaretleme için kullanılabilecek ultra-ince, esnek ve pasif radio frekans (RF) rezonatörleri araştırılmıştır. Klinik uygulamalarda başarıyla test edilen bu cihazın MR görüntüsünde etkili ve güvenli bir şekilde görüntüde iyileşme sağlanmıştır. Ultra-ince ve esnek yapısı sayesinde vücudun çeşitli yüzeylerinde güvenli bir şekilde anatomik işaretleme gerçekleştirilmiştir. Sonuçlar, önerilen yapının düşük arka plan döndürme açılarında yüksek sinyal gürültü oranı ve yüksek işaretleme kontrastı sağlayarak hassasiyet ve hızlı görünürlüğü göstermiştir. Ayrıca, klinik çalışmalarda, önerilen cihazın işaretleme işlevselliği kullanlarak başarılı bir biyopsi prosedürü gerçekleştirilmiştir. İşaretleme ile ilgili bir başka çalışmada, B_1-alanını bozmadan

bölgesel sinyal ve çözünürlüğü artırmak için yeni bir yöntem önerilmiştir. Endokavite MR görüntüleme için indüktif olarak bağlanmamış şekilde pasif RF rezonatörü kullanılmıştır. Fantom ve in vivo deneyler için T_1 ve T_2 ağırlıklı diziler kullanılmıştır. Elde edilen görüntüler, önerilen teknolojinin, cihazın yakınındaki sinyal ve çözünürlüğün iyileştirildiğini göstermiştir. Bu bulgular, bu tezde gösterilen kablosuz algılama ve işaretleme yaklaşımlarını kullanan uygulamalarda yeni imkanlara fırsat tanıyacaktır.

Anahtar sözcükler: Manyetik rezonans görüntüleme, ince-film mikrodalga rezonatörü, indüktif kuplaj, MRG işaretleyici, kablosuz pasif rezonatör, RF uyarma, gerilim algılama.

Acknowledgement

I would like to express my special appreciation and thanks to my advisor Prof. Hilmi Volkan Demir, he has been a tremendous mentor for me. I would like to thank him for encouraging me for research and for allowing me to grow as a research scientist. His advice on my research work as well as on my career have been priceless. I would especially like to express my sincere gratitude to our collaborator and my co-advisor Prof. Ergin Atalar for his continuous support of my Ph.D study and related research, for his patience, motivation, and immense knowledge. His guidance helped me in all the time of research and writing of this thesis. My sincere thanks also goes to Prof. Emine Ulku Saritas, who provided me with an opportunity to work with her team gave access to her laboratory. Without her precious support it would not be possible to conduct my research.

I would also like to thank my committee members, Prof. Yesim Serinagaoglu, Prof. Tolga Cukur, and Prof. Kader Karli Oguz for serving as my committee members even at hardship. I also want to thank you for letting my defense be an enjoyable moment, and for your brilliant comments and suggestions, thanks to you.

I thank my fellow labmate Dr. Volkan Acikel in for the stimulating discussions, for the sleepless nights we were working together before deadlines, and for all the fun we have had in the last five years. Also I thank my friends in the UNAM, UMRAM, ARL, and Bilkent University. In particular, I am grateful to Emre Unal, Sayim Gokyar, Mustafa Utkur, Dr. Evgeniya Kovalska, Dr. Asli Unlugedik, Behnam GasemiParvin, Danzel group, Dr. Ramez kian, Rahim Bahari, Dr. Can Uran, Mohammad Tofighi, Dr. Oktay Algin, Dr. Gamze Aykut, Dr. Cagdas Oto, and Dr. Manuchehr Takrimi. All of you have been there to support me when I required patients and collect data for my Ph.D thesis. I would also like to thank all of my friends who supported me in writing and incented me to strive towards my goal.

Last but not the least, I would like to thank my family: my parents and my sister for supporting me spiritually throughout writing this thesis and my life in general. Words cannot express how grateful I am to my mother and father for all of the sacrifices that you have made for me. Your prayer for me was what

sustained me thus far.

Contents

List of Figures

List of Tables

Chapter 1

Introduction

Rapid progress in thin-film microwave devices has been accompanied by an increasing number of applications of these structures in medical field. The interactions of scientists and engineers with different disciplines resulted in significant advances in medical health care using dedicated and sophisticated equipment. Therefore, the use of RF and microwave devices in practice of medicine has increased. Most of the medical applications of these structures include inductive electromagnetic (EM) coupling into biological tissue, for example, in medical imaging, hyperthermia, and bone fracture healing. These applications can be classified into two categories: diagnosis and therapy. In this thesis we focus on the former one. In diagnostics, EM power is applied to measure, track and/or assess a physiological parameter or to obtain medical images of the body. The microwave structures can be classified as two active and passive devices. In the latter group, wireless passive devices, which avoid the need for any elongated connection or power source, attract more interest.

The objectives of this thesis are to use the advantages of thin film microwave technology to develop thin film microwave resonators for sensing and marking purposes.

The theoretical framework of our thesis study was presented in Chapter 2. We

begin by describing thin-film microwave resonators for wireless sensing. We then discuss about the inductively-coupled resonators for marking in magnetic resonance imaging (MRI). Finally, we explain an inductively receive-only resonator for MRI-endoscopy.

In Chapter 3, we proposed and developed a novel wireless passive RF resonator scheme that enables telemetric strain sensing avoiding the need for calibration at different interrogation distances. The specific architecture of the proposed structure allows for strong inductive coupling and, thus, a higher wireless signal-to-noise ratio. Here, in operation, the frequency scan of the sensor impedance was used to measure simultaneously both the impedance amplitude and resonance frequency. Using this wireless sensor, we further introduced a new telemetric monitoring modality that employs full electrical characteristics of the system to achieve correct strain extraction at any interrogation distance. In principle, any deformation of the sensor structure results in the resonance frequency shift to track strain. However, changing of the interrogation distance also varies the inductive coupling between the sensor and its pick-up antenna at the interrogation distance. Therefore, at varying interrogation distances, it is not possible to attribute an individual resonance frequency value solely to an individual strain level, consequently resulting in discrepancies in the strain extraction if the interrogation distance is not kept fixed or distance-specific calibration is not used. In this work, we showed that by using both the proposed passive sensor structure and wireless measurement technique, strain can be successfully extracted independent of the interrogation distance for the first time. The experimental results indicate high sensitivity and linearity for the proposed system. These findings may open up new possibilities in applications with varying interrogation distance for mobile wireless sensing.

In Chapter 4, we showed a flexible, ultra-thin, and passive RF-based MRI resonator marker with clinical marking feasibility and reliability at various regions of the body. An inductively coupled and implantable wireless RF-based passive MRI resonator marker was constructed. This marker consisted of two patterned metal plates in the shape of connecting rings, deposited on both sides of a dielectric substrate, which provides distributed inductance and capacitance along

the conductive lines, where upper and lower rings were connected to each other through a via metallization. A 3T MRI marking procedure was experimented in phantom and ex vivo, and then the marker performance was evaluated by human MRI experiment. Results show that, at low background flip angles, the proposed structure enables precise and rapid visibility with high marker-to-background contrast as well as high signal-to-noise ratio. Also clinical studies show a successful biopsy procedure using marking functionality of our device. The ultra-thin and flexible structure of this wireless flexible RF resonator marker offers effective and safe MR visualization with high feasibility and reliability of anatomic marking and guiding at various regions of the body.

In Chapter 5, we proposed and demonstrated a method of decoupling our RF resonator from transmit RF field by using a dual-drive birdcage coil. The RF resonator coupled to the receive coils resulting in SNR improvement without causing flip angle inhomogeneity. When the orientation of a linearly-polarized excitation of RF magnetic field becomes orthogonal to the normal vector of an RF resonator, no current induction is expected. With this field, however, excitation is still possible. On the other hand, if the receive coils couple to the resonator, MR signal enhancement becomes possible. The proposed transmit decoupling method results in preventing flip angle inhomogeneity and reducing safety concerns without using bulky decoupling diodes on the RF resonator. In our implementation, a resonator was tuned to the operating frequency of 3T MRI scanner using thin-film microwave techniques. The resonator was rolled on an endocavity probe. A dual-drive body birdcage coil was used for weighting amplitudes of the feeding ports steers the direction of the linearly- polarized B1-field to decouple the resonator from transmit field and operate the resonator in receive-coupled mode. During reception of the MR signal, the resonator was coupled to receive coil and results in SNR enhancement at the vicinity of the resonator. T_1- and T_2-weighted sequences were employed for phantom and in vivo experiments. The images show the feasibility of the proposed structure and techniques to improve the SNR and resolution at the vicinity of the device without flip angle inhomogeneity.

In Chapter 6 , we finally conclude the dissertation summarizing and discussing our achievements in this thesis and future prospects.

Chapter 2

Theory and Methodology

2.1 Inductively-Coupled Wireless Sensing

In our system, the principle of wireless monitoring based on inductive coupling is illustrated in Figure 2.1. We include all the electrical components that come from the system (e.g., cable, connector, and antenna) to determine the accurate resonance frequency of the sensor. All the impedance parameters of these components were calculated, and their effects were taken into account in the resonance frequency extraction. Z_{eq1}, Z_{eq2}, and Z_{eq3} are the impedances that are seen at the input of cable-connector, cable-connector-antenna, and cable-connector-antenna-sensor, respectively.

The inductive coupling between the sensor and the reader antenna affects the impedance at the input of the antenna [1]. Since the sensor impedance Z_s reaches a minimum at its resonance frequency (f_0), this provides maximum impedance, which appears at the input of the antenna at f_0. By scanning the variation on the equivalent impedance, monitored by the reader antenna, the resonance frequency can be extracted. Assuming an inductive coupling between the sensor and reader antenna, the sensor impedance Z_s, measured by the reader antenna is given by

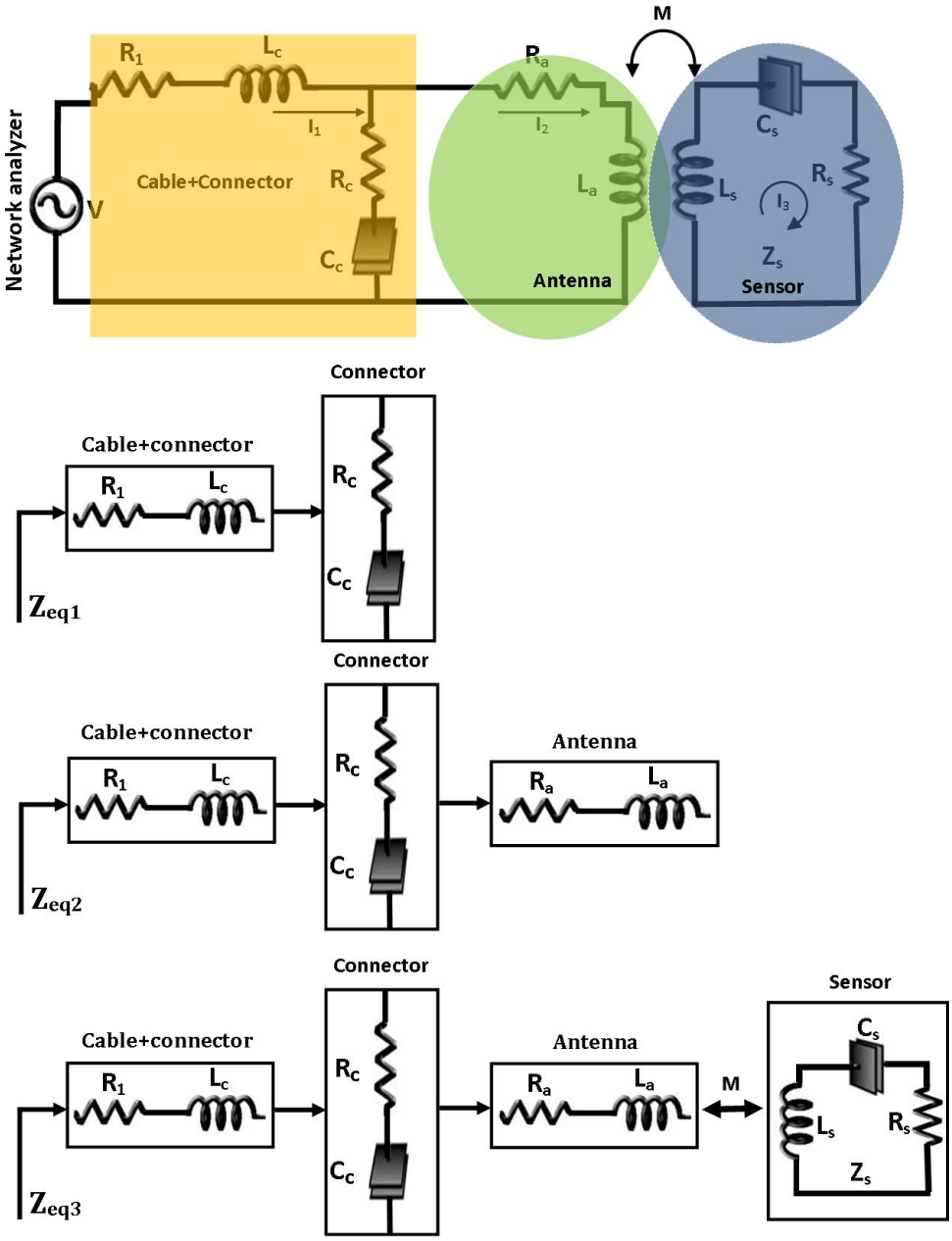

Figure 2.1: Schematic of the proposed system. The sensor is inductively coupled to the pick-up reader antenna. To obtain the exact value of the resonance frequency (f_0) of the sensor, all the resistance, capacitance and inductance values induced by the cable, the connector, and the antenna are included.

$$V = \{(R_1 + jwL_c) + [(R_c + \frac{1}{jwC_c}) \parallel (R_a + jwL_a - \frac{jwMI_3}{I_2})]\} \tag{2.1}$$

where M is the mutual coupling coefficient between the sensor and the pick-up antenna,

$$(R_s + jwL_s + \frac{1}{jwC_s})I_3 = jwI_2 \tag{2.2}$$

$$(R_s + jwL_s + \frac{1}{jwC_s}) = Z_s \tag{2.3}$$

From (2.1) and (2.3);

$$Z_{eq} = \frac{V}{I_1} = (R_1 + jwL_c) + [(R_c + \frac{1}{jwC_c}) \parallel (R_a + jwL_a + \frac{w^2M^2}{Z_s})] \tag{2.4}$$

$$Z_s = \frac{w^2M^2(R_1 + jwL_c + R_c + \frac{1}{jwC_c} - Z_{eq})}{(Z_{eq} - R_1 - jwL_c)(R_c + \frac{1}{jwC_c} + R_a + jwL_a) - (R_c + \frac{1}{jwC_c})(R_a + jwL_a)} \tag{2.5}$$

The resonance frequency of the sensor is determined by scanning the frequency response of the sensor impedance, Z_s. When the sensor stays in the interrogation region of the pick-up reader antenna, a net resonance comes along at the operating frequency of the sensor [2]. The variation of the coupling value would lead to a change in the impedance Z_s and, consequently, the shift of the system resonance frequency [3]. Any mechanical variations on the sensor, for example deformation due to strain, can be faithfully detected using the associated electrical characteristics (f_0 and $|Z_s|$) changes, which are picked up by the reader antenna. Each (f_0 and $|Z_s|$) set point is devoted to an individual strain value, assuming that no other physical parameter changes. Thus, using both frequency

and impedance information together strain can be calculated independent of the coupling value.

Here, note that the proposed sensor has two main elements: (1) the split ring capacitors between the fingers, which are the sensing components, and (2) the split rings inductor, which collects electromagnetic energy from antenna.

2.2 Inductively Transmit/Receive-Coupled Wireless Marking

The wireless resonator studied for marking has two significant components; namely, inductor (L), which is introduced as a passive power source in the form of conductive paths, and the distributed capacitor (C), which is the dielectric layer sandwiched between the conductive paths. In the case of using magnetic resonance imaging, electromagnetic energy radiated by the transmit RF coils is inductively coupled the resonator resulting in a secondary EM radiation from the resonator to re-align the spins in its immediate vicinity, hence resulting to effective excitation angle amplification.

Inductive coupling between the RF resonator marker, which is tuned to the Larmor frequency, and the MR transmitter and receiver coils leads to local MR signal enhancement in the surrounding medium of the marker. The fundamental principle of local signal enhancement originates from the basis of effective flip angle increasing around and inside the resonator marker during the RF excitation and signal amplification during reception. During RF excitation, the marker locally amplifies the excited angle, and then the enhanced MR signal is picked up by receiver coils. MR signal detected by the resonator marker is brighter whereas, background presents very poor signal, which leads to high marker-to-background contrast. Figure 2.2 illustrates the operating principle of wireless passive RF resonator marker. The external magnetic flux Φ_{rf} of the transmit coil inductively couples to the resonator probe [4]. The reaction of the resonator

with external flux leads to circulating current in the resonator, which results in a flux Φ_{re}. Therefore, the total flux Φ_t around the resonator can be written as:

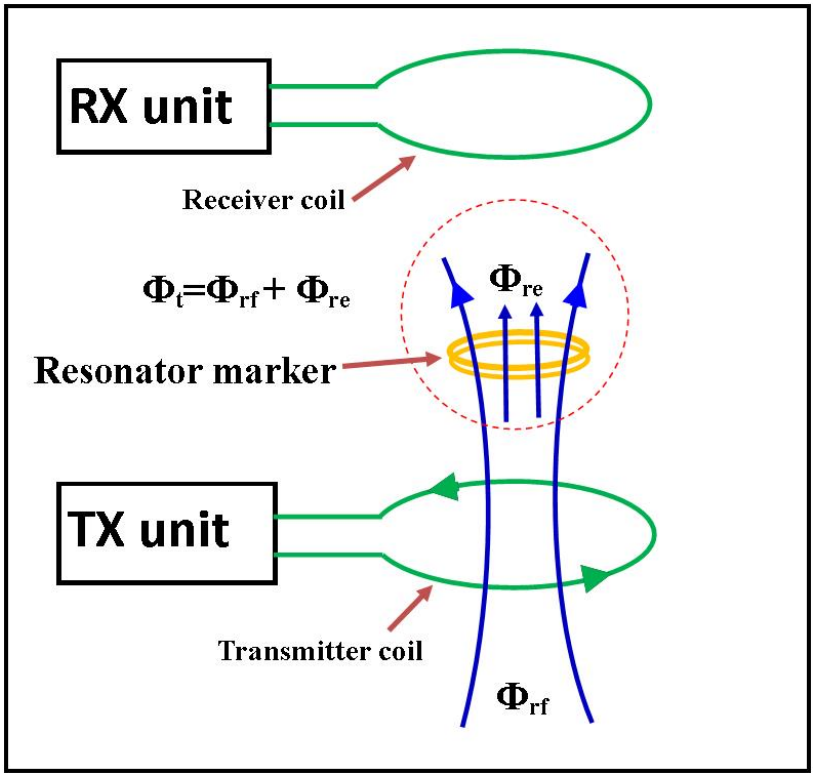

Figure 2.2: The operating principle of wireless passive RF resonator marker. In RF excitation mode, the resonator marker, which is tuned to the resonance frequency, locally amplifies the flip angle. In RF receiver mode, the resonator marker picks up the amplified magnetization in its immediate vicinity, resulting in magnified magnetic field that can be inductively coupled to receiver coils.

$$\Phi t = (\frac{R + iwL}{R + iwL + \frac{1}{iwC}})\Phi rf \tag{2.6}$$

If

$$w = w_0 = \frac{1}{\sqrt{LC}}, \tag{2.7}$$

then

$$\Phi t = (\frac{R + iw_0 L}{R})\Phi rf = (1 - iQ)\Phi rf = \Phi rf + \Phi re \tag{2.8}$$

where i represents a quadrature phase relationship between the transmit field B_1 and the field generated by the resonator and $Q = \frac{w_0 L}{R}$ is the resonator quality-factor. R is the resistance of the resonator.

Φ_{re} is the additional flux provided by the resonator inductance that is added to the original flux Φ_{rf}. This external flux leads to extra excitation field $\mathbf{B}_{re}$ which alters the effective flip angle (FA) by position. In other words, according to the Faraday's law of induction, the nuclear magnetic resonance signal detected by the receiver coil in the regions of interest is:

$$S(t) = -\frac{\delta}{\delta t} \int \mathbf{B}_{re}(x, y, z).\mathbf{M}(x, y, z)\, dv \tag{2.9}$$

where $\mathbf{B}_{re}(x, y, z)$ is the produced magnetic field at a position (x,y,z) by unit current passing through the coil base on the principle of reciprocity [5, 6]. Additional excitation $\mathbf{B}_{re}(x, y, z)$-field generated by the resonator marker increases the signal intensity near the resonator. It can be written as follow:

$$S(t) = -\frac{\delta}{\delta t} \int [\mathbf{B}_{rf}(x, y, z) + \mathbf{B}_{re}(x, y, z)].\mathbf{M}(x, y, z)\, dv \tag{2.10}$$

FA amplification and receiver coupling improvement are achieved by using inductive coupling to both the receiver and transmitter coils.

For an optimal signal enhancement in immediate vicinity of the resonator marker, resonator axis must be perpendicular to the static magnetic field of the scanner. Effective FA dependence on the tilt angle is one of the drawbacks for wireless resonator markers. Despite of this limitation, our resonator design with high Q-factor characteristics and flexible structure presents better performance in curved configurations while the marker is not perpendicular to the direction of main magnetic field.

2.3 Inductively Receive-Only Coupled Wireless Endoscopic Probing

Inductive coupling between the RF resonator and the MR transmitter/receiver coils leads to local MR signal enhancement at the vicinity of the resonator probe. The fundamental principle of local signal enhancement originates from two basic concepts: first, FA increase around the resonator during RF excitation due to the coupling between the transmit coil and the resonator; and second, the amplified MR signal during reception due to the coupling between the resonator and the receive coil [7, 8].

The magnetic field generated by the resonator is dominant at its close proximity, consequently giving rise to local FA amplification. FA amplification during spin excitation disturbs the B_1^+ homogeneity around the resonator. The coupling between the transmit coil and resonator can also lead to safety problem. Dual-driven birdcage coil can steer the B_1-field to provide the possibility to decouple the resonator during spin excitation. Excitation decoupling leaves the signal amplification only in reception mode to eliminate the B_1^+ inhomogeneity problem and also the possible safety concerns.

Conventional birdcage coils have two orthogonal transmit ports located physically 90^0 apart from each other. If only one port is fed, a linearly-polarized (LP) magnetic field is generated in the corresponding direction, and the other port generates a field perpendicular to the first one. Conventionally birdcage coils are driven with quadrature excitation through two ports, and generates a circularly-polarized field. However, when these two ports driven in phase by weighting the amplitudes, an LP field with desired direction can be generated (Figure 2.3) [9–11].

When the RF transmit field is LP, coupling of the excitation field and the resonator is directly related to the applied magnetic field orientation. Steering the generated LP RF excitation can decouple the resonator probe from RF excitation filed and leaves the resonator in receive-only coupled mode. In receive-only

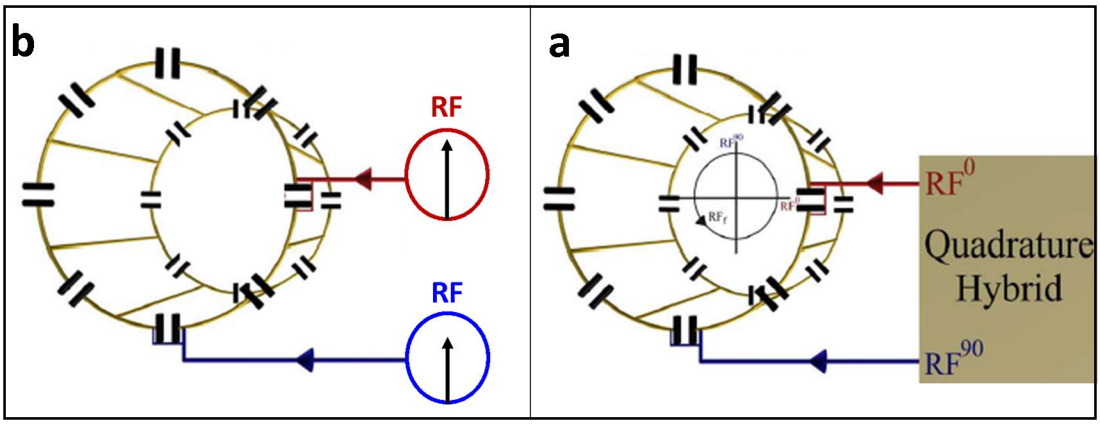

Figure 2.3: (**a**): Conventional hybrid quadrature birdcage coil that is used for forward-polarized excitation. The input signal of the channel are in 90^0 phase difference. (**b**): Dual-drive birdcage coil excitation that is used to steer the applied RF field to decouple the resonator from excitation field.

coupled mode, the rotating magnetic field generated by excited spins induces a current on the resonator coil that resulted in a magnetic field around the resonator. The generated magnetic field by the resonator magnifies the collected signal by receiver coil.

Chapter 3

Inductively-Coupled Wireless Sensing

This chapter is based on publication "Development of a distance-independent wireless passive RF resonator sensor and a new telemetric measurement technique for wireless strain monitoring" A.Alipour, E.Unal, S.Gokyar, and H.V.Demir, *Sensors and Actuators A: Physical, 255, 87-93, 2017.* Reproduced (or 'reproduced in part') with permission from Elsiver publications.

3.1 Introduction

Precise strain monitoring is essential in numerous strain sensing applications including implants, food quality control, and structural health monitoring [12–14]. Over the past few decades, enormous progress has been achieved in wireless passive and implantable strain monitoring techniques. Their wireless readability, low cost, power source-free operation, and low perturbation from the surroundings are among the main advantages of the wireless passive approaches over common active ones [15, 16]. In telemetric strain sensing, the ability to wirelessly track the

passive resonance is of critical importance [17]. The fundamental operating principle of wireless sensing results from inductive coupling between the passive RF resonator and its reader antenna [1]. The concept of such passive RF resonators using different electromagnetic structures has been proposed and demonstrated for the purpose of wireless strain monitoring. Since the electromagnetic resonance frequency of a resonator is sensitive to its physical dimensions, any deformation in its geometry results in resonance frequency change [3]. The most recently studied architecture for wireless passive strain monitoring includes micro-strip patch antennas, radio frequency identification (RFID), and metamaterial-based RF resonators. The feasibility of using a circular micro-strip patch antenna (CMPA) was reported by Daliri et al. [2]. Using theoretical calculations and numerical simulations, the authors showed a linear relationship between the strain and the resonance frequency of the proposed system. Any change in the dimension of the CMPA structure changes the impedance of the system, which leads to the shift in resonance frequency. A complementary work on CMPAs was reported in [18]. It was shown that CMPAs can be used as a passive sensor for wireless strain monitoring in civil structures and aerospace. The effect of the conductivity of the host material on the wireless measurement efficiency was also investigated. It was demonstrated that strain can be monitored wirelessly in any desired direction using a linearly polarized horn antenna. However, due to the sensor signal interference with background reflections, only a limited interrogation distance was achieved. RFID structures have also been investigated for wireless passive strain measurements. The RFID-based wireless sensors are fed by interrogation electromagnetic wave radiated from a reader antenna. Xiaohua et al. [19] developed a passive wireless antenna sensor for strain and crack detection. The antenna signal modulation was used to isolate the backscattered signal from the undesired environmental reflections. From the previous works of our group, Melik et al. [20, 21] proposed a highly sensitive metamaterial-based strain monitoring technique to track bone fracture healing. This sensor consists of double comb-shaped multiple split ring resonators (SRRs). The compact nested architecture of this SRR design with multiple gaps provides a lower operating frequency and higher sensitivity. In operation, the wireless passive metamaterial strain sensor is mounted on an implantable fracture fixation hardware to monitor and access

the progression of bone fracture healing. When an external load is applied to the hardware, the strain is recorded remotely using the coaxial probe located in the proximity of the sensor. This sensor can measure strain based on the change in the capacitance of nested SRR that results in the transmission spectrum shift. The in vivo results showed that the metamaterial-based passive strain sensor provides the ability to determine statistically important difference between the fracture healing and non-healing groups [22]. However, these sensors are resonant structures without a ground plane, so they exhibit relatively low SNR ratio and quality factor. Our group also developed another metamaterial-based remote strain sensor system using an array of the SSRs patterned over a flexible Kapton gold clad substrate [23]. This approach was limited by the weak reflected signal from the sensor to the reader antenna. In most of these studies, misalignment and variation in interrogation distance can change the transmission spectrum, consequently leading to inaccurate strain extraction. To overcome this problem, in this paper, we propose a distance-independent passive RF resonator sensor and a new telemetric measurement methodology for its wireless strain monitoring. Here the comb-shape split rings are patterned on both sides of the flexible dielectric to form a distributed capacitance and inductance tank circuit. The combination of the capacitance and inductance creates an LC resonator to operate at a certain frequency. The comb-shape split rings are aligned by 90^o rotation with respect to each other on both sides of the dielectric. This specific architecture of the sensor allows for the possible excitation of both of the layers by the same incoming electromagnetic wave. Thus, both of the layers contribute to the resonance frequency and the quality factor of the structure. We also introduce a new measurement technique of wireless strain sensing which, in combination with the proposed sensor, strain can be monitored independently of the interrogation distance. Based on this approach, possible discrepancies induced by the coupling coefficient variations are eliminated in the strain extraction. Experimental results indicate great linearity and sensitivity.

3.2 Method

3.2.1 Sensor Resonator

The design of the strain sensor relies on the resonance characteristics, especially the resonance frequency, f_0 and the quality-factor, Q, which are functions of the sensor capacitance (Cs), inductance (Ls), and resistance (Rs). A simple geometry of the proposed strain sensor with seven geometrical variables is shown in Figure 3.1a. The values of Cs, Ls, and Rs are determined by these design parameters: number of fingers n, gap width s, fingers spacing t, sensor length k, line width w, short fingers length l1, and long figures length l2. The sensor is modeled to

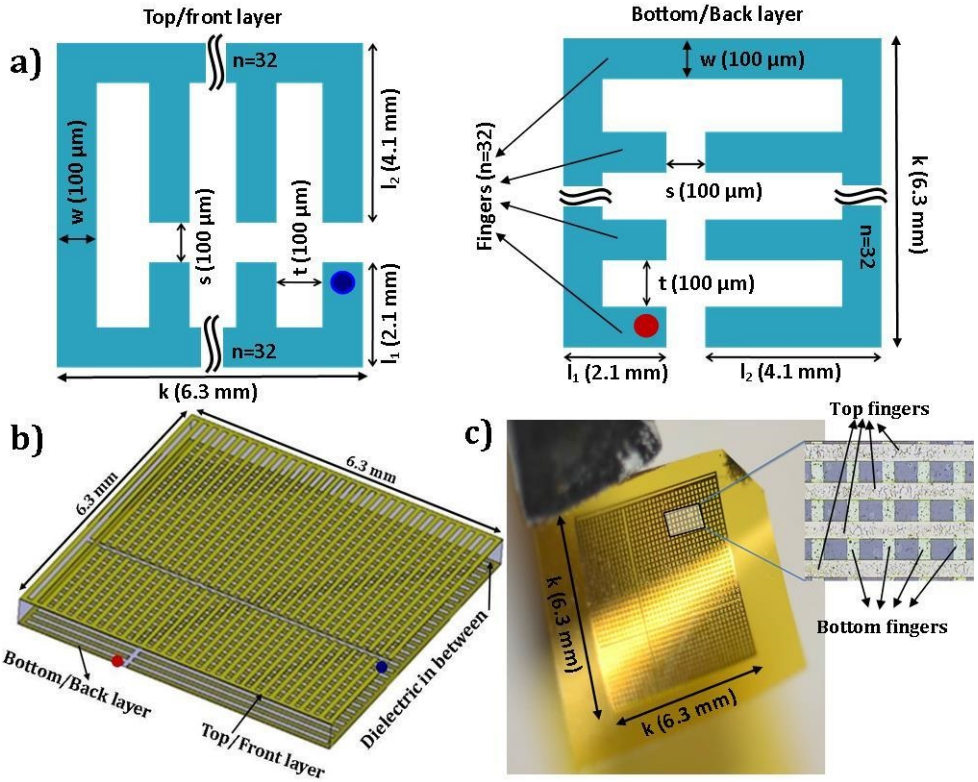

Figure 3.1: (**a**). Simple sensor geometry, the top layer (left) and the bottom layer (right). The bottom layer is 90^o rotated with respect to the top layer. (**b**). 3D schematic of the proposed strain sensor (not drown to scale). Red and blue dots on the sensor geometry coincide with the same points on the 3D schematic, which are shown with the same colors. (**c**). Optical image of the fabricated flexible strain sensor.

operate as an electrical LC resonant circuit. Figure 3.1b shows a 3-dimensional (3D) sketch of our proposed strain sensor. The top/front side of the device includes a layer of comb-shaped SRRs metallization. The bottom/back side of the device is the 90^o rotated version of the top/front side that is patterned on the other face of the dielectric substrate. This architecture brings us two main advantages: first, it allows electromagnetic wave to penetrate through the upper layer and bottom one. Accordingly, with proper polarization, both of the layers can be excited by the same incoming electromagnetic wave. Thus, both layers contribute to the operating frequency and Q-factor of the device. Second, due to symmetric structure of the sensor, strain can be measured in any direction. The sensor has inductance Ls and capacitance Cs. Cs is the combination of the split (metal-air-metal) and sandwiched (metal-substrate-metal) capacitors that build up from the sensor architecture. The integration of capacitance Cs with inductance Ls forms a resonance circuit. The corresponding resonance frequency is simply

$$f_0 = \frac{1}{2\pi\sqrt{L_s C_s}} \tag{3.1}$$

The Q-factor of the sensor affects the precise wireless identification of the sensor resonance frequency. High Q-factor results in strong inductive coupling and the larger interrogation distance. To increase the power reflected by the sensor, the Q-factor of the sensor is increased by improving the structural parameters of the sensor. The metal thickness is one of the main parameters that can control the Q-factor, consequently the reflected power. To maximize the reflected power back to the antenna, the metal thickness is set to be two times thicker than the electrical skin depth [24]. The well-known equation to calculate the skin depth is given bellow:

$$\delta = \sqrt{\frac{1}{2\pi f_0 \sigma \mu_0 \mu_R}} \tag{3.2}$$

where σ is the conductivity (m^{-1}), μ_0 the permeability constant ($4\pi\ times10-7$ H/m), and μ_R the relative permeability. For the target operating frequency of our proposed strain sensor ($\sim$ 600 MHz), the skin depth of gold is calculated to be ~ 3 μm . The investigations of the gold skin effect on the Q-factor at the operating frequency shown that the Q-factor is increased by the increasing metal thickness, and becomes fixed after ~ 6 μm metal thickness. Thus, in this study, the gold

thickness of 6 μm was used in the sensor fabrication. During the operation, when the sensor is subjected to strain ε in each direction, the geometrical deformation on the sensor leads to change in the split ring capacitance (between fingers) values, which results in the resonance frequency shift. The variation of capacitance values contribute to the resonance frequency shift and, consequently strain sensing.

Our proposed architecture is based on a multilayer laminated structure consisting of two comb-shaped SRRs, which are patterned on both sides of the dielectric substrate, with 90^0 alignment with respect to each other (Figure 3.1). We fabricated our strain sensor using standard microfabrication technique. The fabrication processes include the following steps: (1) Thermal evaporation was used to deposit a thin layer of Au on both sides of the flexible dielectric substrate (Kapton polyimide films, DuPont). (2) Conventional lithography and wet-etching were used to pattern the Au layers of comb-shaped SRRs on both sides of 25-μm-thick Kapton. Finally, a flexible sensor with the thickness of $\sim 37\mu m$ was obtained. A photo of the fabricated sensor on the flexible Kapton film and the corresponding optical image are displayed in Figure 3.1c. Due to the flexibility and ultra-thin structure of the sensor, the sensor has the capability to conform to various non-planar surfaces.

3.2.2 Sensor Characterization

Our experimental setup utilized for the telemetric strain monitoring is shown in Figure 3.2. The fabricated sensor is set on the host structure to characterize the sensor performance in strain measuring. The host structure is a homo-polymer rod; namely, Delrin with dimensions 1.2 cm $\times$1.2 cm $\times$10.0 cm and Youngs modulus of 2.4 Gpa. The axial tensile force of 2 kN was applied to the system in four loading steps with 500 N load increment per step using a tensile tester machine (INSTRONTM 5542). To verify the uniform strain induction in the area where the sensor is mounted, a standard resistive strain gauge (Tokyo Sokki Kenkujo Co., Ltd.) is set to the host structure as shown in Figure 3.2. The strain gauge is positioned on the other side of the Delrin, which does not affect the sensor

performance. The test starts with 0 $\mu\varepsilon$ initial load and ends at around 21,300 $\mu\varepsilon$. The impedance of the strain sensor is measured at the various interrogation distances using the pick-up coil (with 8 mm in diameter) as the reader antenna under each loading step. The reader antenna is mounted on a 3D stage machine

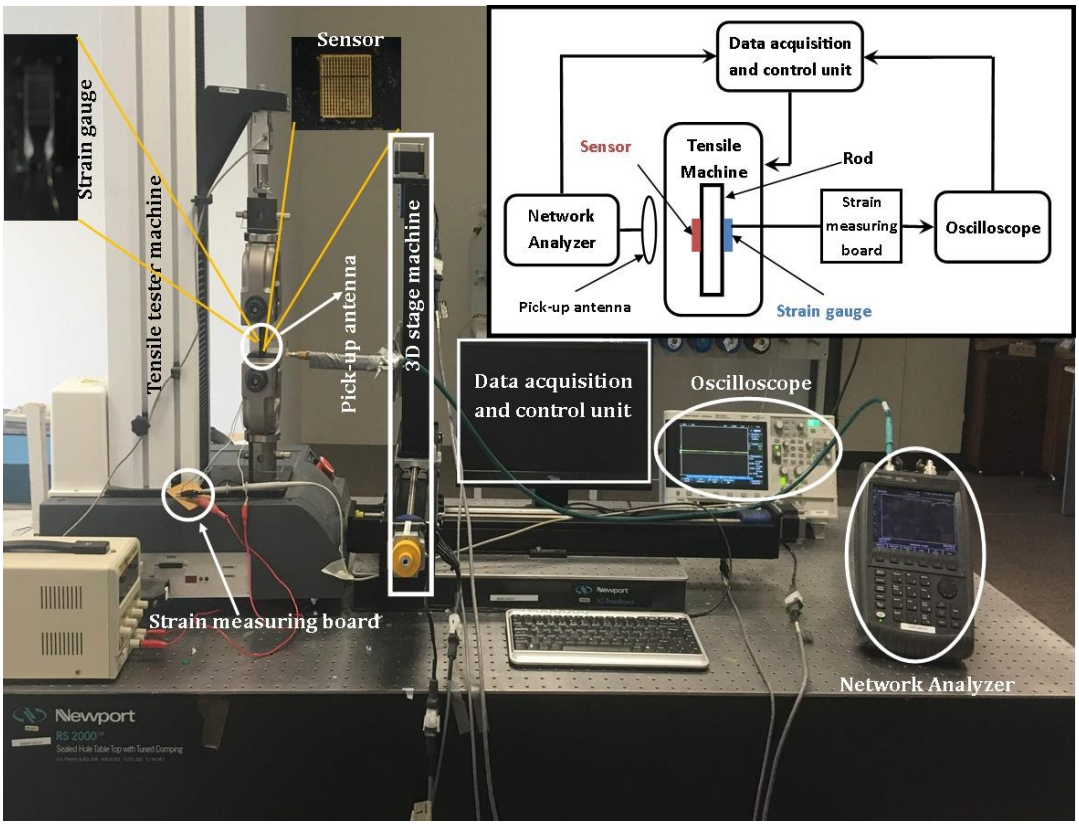

Figure 3.2: Experimental setup. The strain sensor is set on the homo-polymer rod (Delrin), a pick-up antenna is used to read the sensor signal, a commercial strain gauge is placed at the opposite sides of the rod to verify the strain value, and a 3D stage machine is used to scan the interrogation distance precisely. On top right we show the block diagram of the passive wireless strain sensing setup. Network analyzer was arranged in the frequency range between 540 MHz and 700 MHz with 1601 data points. The axial tensile force at various loads was applied to the system and then obtained data of network analyzer was collected at each interrogation distance.

(WELMEX, Inc.). The stage automatically interrogates the region step by step. We used a network analyzer (Agilent FieldFox N9915A) as the signal acquisition instrument that was arranged in the operating frequency range with 1601 data points. The experiment was conducted at ten interrogation distances from 0.5

to 3.0 mm. The sensor with following design parameters was used in the strain measuring experiment: n=32, s=100 μm, t=100 μm, k=6.3 mm, w=100 μm, l1=2.1 mm, and l2=4.1 mm.

3.2.3 Results and Discussion

Before studying the strain sensor performance, the effect of interrogation distance was investigated. As it has been expected, changing the interrogation distance the level of inductive coupling between the sensor and the pick-up antenna varies, as shown in Figure 3.3. Due to the coupling coefficient variation, the system operating frequency changes at various interrogation distances. The variation in the operating frequency can be larger than the shifts caused by the applied load. Therefore, it becomes impossible to attribute an individual resonance frequency value to an individual strain value, consequently resulting in discrepancies in the strain extraction, unless specific calibration curves are used at specific fixed interrogation distances. To solve this problem, the sensor was tested under different load values and varying interrogation distances to find relation between the strain, $|Z_s|$, and f_0. Here both the frequency and $|Z_s|$ information are used to extract the individual strain value. Figure 2.4a shows the resonance frequency variation by changing the inductive coupling coefficient (by changing the interrogation distance) under various strain values. Here, x axis is represented in terms of Real$\{M^2/Z_s\}$ to better understanding the measured resonance frequency variation with respect to the various coupling levels. This figure also shows a clear resonance frequency increase with the increasing coupling coefficient.

To investigate the tensile strain response of the sensor as the strain increases, the resonance frequency is measured at different strain values. The relation between the resonance frequency shift of the sensor and strain is displayed in Figure 3.4. This plot confirms that the measured resonance frequency of the sensor at various load values exhibits a characteristic linear response. The measured resonance frequency of the sensor gradually increases as the strain increases. The resonance frequency of the sensor at 0 $\mu\varepsilon$ is around 591 MHz, and then it reaches

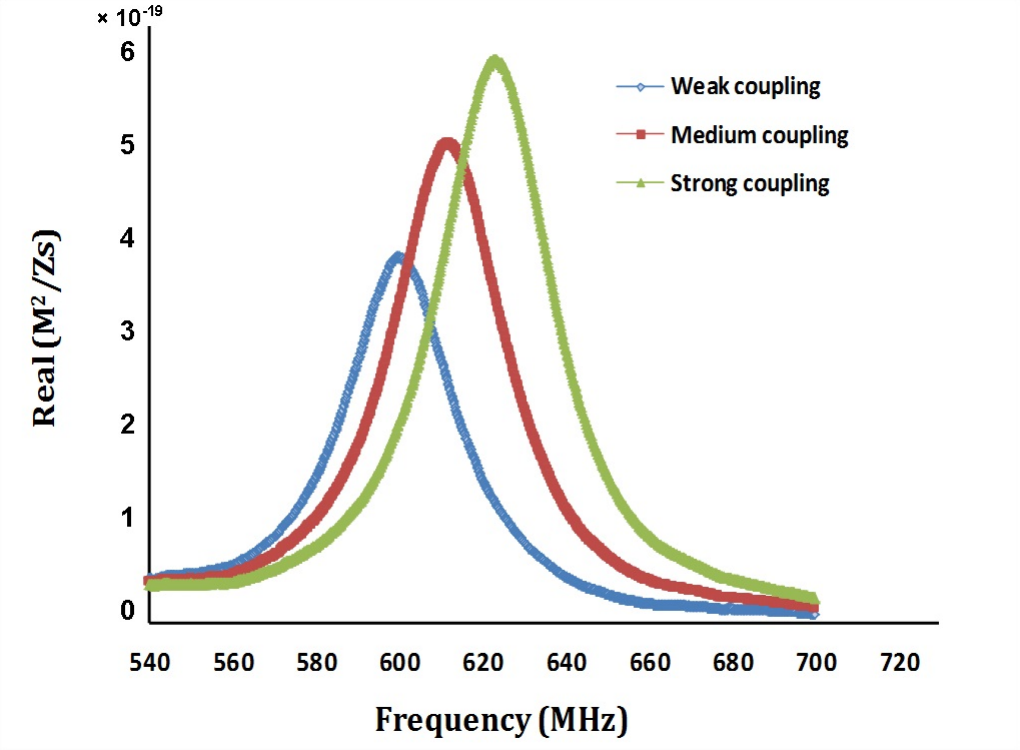

Figure 3.3: By changing the inductive coupling (by varying the interrogation distance) between the reader antenna and sensor, the operating frequency of the system and impedance of the system (Z_{eq4}) were changed. The strong coupling, medium coupling, and weak coupling correspond to the distances of 0.5 mm, 1.3 mm and 2.4 mm far from the pick-up antenna, respectively.

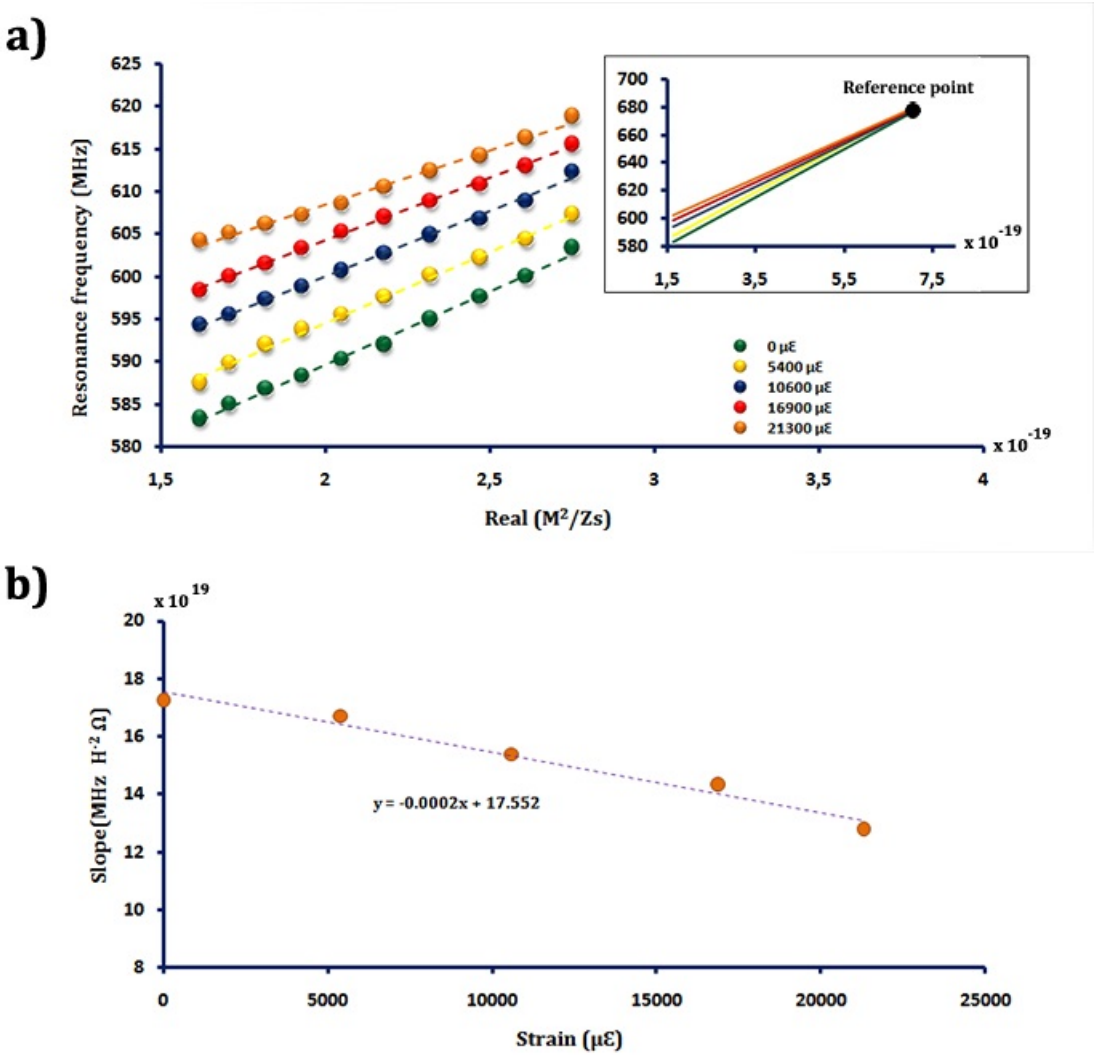

Figure 3.4: (**a**): Resonance frequency variation under different strain levels at different interrogation distances. Linear fits at various strain values intersect at a common interpolated reference point. Due to close proximity of the sensor and reader antenna (dominant coupling effect), measured signals tend to intersect at this point at different strain levels. (**b**): The calculated slope of any measured point with the reference point corresponds to an individual strain value (measured by strain gauge).

approximately to 597 MHz, as the strain increases up to 10,500 $\mu\varepsilon$. The experimental results show that the sensor achieves successful strain performance with the high sensitivity. Due to the proximity of the sensor and pick-up antenna, mutual coupling is more dominant, which does not allow for the significant resonance frequency change by the strain variation. Strong coupling between the sensor and the antenna at this point allows all linear fits at various strain levels (Figure 3.4a) tend to a single intersecting point which we call Reference Point here. Figure 3.4b shows the slope values of these linear fits at various strain levels, measured by the strain gauge. Any measured set point (f_0 and $|Z_s|$) creates a slope by the Reference Point. This slope gives the extracted strain value.

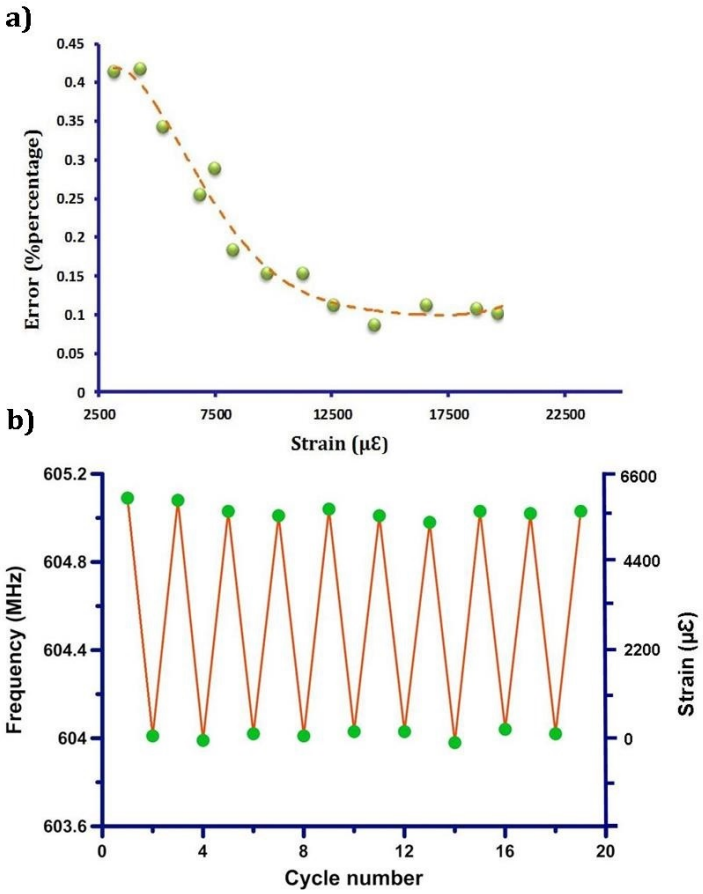

Figure 3.5: (**a**): Nonlinearity error percentage. At high strain values error was minimized. (**b**): The multicycle operation of the sensor between the two strain states (achieved by strain gauge) showed that the response of the sensor is stable and reliable.

After the strain characterization and analyzing the relationship between the

strain and set point (f_0 and $|Z_s|$), similar tensile test is conduced to investigate the sensor performance and verification. The sensor was subjected to a random set of strain levels and interrogation distance values. The experimental error analysis in Figure 3.5a exhibited excellent sensor performance. The fitted curve in this figure reports a maximum error of only less that 0.5 % corresponding to nonlinearity error at the early stages of the strain implementation. This could be largely explained by the dominant effect of the uncorrelated measured strain between the strain gauge and our sensor. Also, some part of this error stems from the strain gauge voltage measurement error. By increasing the strain, calculated error was minimized, which could be explained by the dominant effect of the applied strain. The resonance frequency and $|Z_s|$ of the sensor can be interrogated by the pick-up antenna in the range of 3 mm. Beyond this distance, due to the very low coupling efficiency, the reader antenna is not be able to sense the signal reflected back from the sensor. Therefore, this distance is the largest operating range for our system. To investigate the effect of the direction of the applied load on wireless strain measurement, the experiment was conducted at two different sensor orientations. The strain was applied in both x and y directions. Due to symmetric structure of the sensor, the experiments resulted in the same behavior. The stability and reliability of the sensor were studied by multicycle strain performing on the sensor. The sensor was first subjected to zero strain loading and then followed by extension loading of 5,400 $\mu\varepsilon$. As shown in Figure 3.5b, these steps were repeated 20 times. The plot of the repeatability showed that the sensor showed excellent stability and reliability, with only slight drifts (0.01 %) observed between the cycles.

3.3 Summary

In this chapter of thesis, we showed that by using both the proposed passive sensor structure and wireless measurement technique, strain can be successfully extracted independent of the interrogation distance for the first time. The experimental results indicate high sensitivity and linearity for the proposed system.

These findings may open up new possibilities in applications with varying interrogation distance for mobile wireless sensing.

Chapter 4

Inductively Transmit/Receive-Coupled Marking

This chapter is based on publication "An Inductively coupled ultra-thin, flexible and passive RF resonator for MRI marking and guiding purposes: clinical feasibility "A.Alipour, S.Gokyar, O.Algin, E.Atalar, and H.V.Demir, *in submission to MRM.*

4.1 Introduction

Anatomical position marking, or interventional tracking, is a major challenge and significant problem for MRI. Solution of this problem normally requires a MR-visible object that precisely presents a reference location, as well as real-time visualization [25, 26]. MR-visible markers are not only one of the most preferred tools for referencing purposes but have also gained considerable interest as a modality to guide medical instruments including biopsy needles for minimally invasive interventions [27]. The basic principle of MR-visible markers relies on

introducing special contrast with respect to the morphological MR images [28,29]. Intrinsic artifacts of MRI-guided needles or tracking devices were the foundation of earlier marking techniques [30–32]. Recently, efforts have focused mostly on MRI visibility and detectability improvement of the marking devices [33–35]. Moreover, identification and marking of MR-visible objects have also introduced a possible solution to reduce motion artifacts [36] and automatic three-dimensional (3D) localization [37].

According to their structure and detection technique, MR-visible markers can be classified as material-based markers or RF-based markers. Material-based markers are either paramagnetic materials, which change local signal by local field distortions [5], or contrast agents, which shorten T_1 or T_2 values of the tissue and alter the MR signal intensity locally [38]. Although this technique avoids possible RF safety hazards, they are not visible for all imaging parameters [30]. RF-based markers can also be categorized into two types; active RF-based markers or passive RF-based markers. Active techniques use small pick-up RF coils that are connected to the MR scanner trough electrically conductive wire. Fast and accurate positioning can be obtained by multiple active markers connected to separate receiver channels. However, a possible safety hazard is introduced by electric coupling between the long connecting wires and transmitter coils [39–41]. Furthermore, the interface to the receiver and crosstalk between the wires are another significant problem. These problems limit the clinical implementation of the active design [4, 42].

To simplify clinical implementation of RF-based markers and avoid possible safety hazards, passive RF-based markers based on inductively-coupled RF coils were reported [9, 43, 44]. These wireless passive RF-based markers use simple resonant LC circuits that are made of lumped electrical components including RF-coils and chip-scale non-magnetic capacitors. These markers do not need any elongated conductors to carry the RF signal. The signal is transmitted and received by inductive coupling to standard transmitter/receiver MR coils. For this purpose, passive RF-based markers are tuned to the resonance frequency of the MR scanner. MR visibility of these markers results from the local MR signal amplification through FA enhancement during RF excitation and signal

enhancement during signal acquisition that leads to special positive contrast. Consequently, a higher marker-to-background contrast is achieved at very low FA.

Due to the requirement for quick position detection, until now, studies have been reported to use passive RF-based markers that provide robust localization. However, the size and rigid structure of these passive markers limit them to be used on critical regions of the body for marking purpose. To overcome these disadvantages we developed a flexible, ultra-thin, and implantable wireless passive RF-based resonator marker. This proposed marker basically consists of two conducting lines, deposited on both sides of its dielectric substrate, which ensures distributed capacitance along the conductive lines, where the upper and lower rings are connected to each other through a via through the substrate [45].

In this work, we show the clinical feasibility and reliability of anatomic position marking using our proposed passive RF-based marker. Ultra-thin structure and flexibility of this marker allow for an opportunity to demonstrate marking at various regions of the body. Here, high performance characteristics of the developed marker were evaluated to enable precise and rapid positioning of the marker for biopsy needle guidance under clinical MR imaging. The marker performance was evaluated in a 3T MRI scanner on phantom, ex vivo animal models, and in clinic.

4.2 Method

4.2.1 Marker Resonator

Recently, we have designed an ultra-thin and flexible passive RF-based resonator to be utilized as MR-guided marker. Our design consists of a resonant helical structure with incorporated layered capacitors to achieve resonance. The developed passive marker has two significant components, namely a distributed inductor introduced as a passive power source in the form of conductive paths,

and the distributed capacitor, which is a dielectric layer sandwiched between two conductive paths (Figure 4.1a). Our proposed device architecture is a multi-layer laminated structure consisting of two broadside-coupled split ring resonators (SRR) [6]. Standard microfabrication technique was employed to pattern 3-μm thick gold (Au) layers on both sides of 7-μm thick polyimide film (Kapton HN, DuPont, Berlin, Germany) where the upper and lower layers are connected to each other through a via metallization. The thin-film resonator marker has a square shaped double-turn coil design with a line length of 8 mm and a line width of 1 mm (Figure 4.1b). In order to obtain electrical isolation, biocompatibility, and to avoid the capacitive effects resulting from the interaction between the resonator marker and the surrounding tissue, the resonator was coated with 50-μm thick polydimethyl siloxane (PDMS) layer on both sides. PDMS (Dow Corning Sylgard 184 Silicone Elastomer, sigma-Aldrich, Germany) is a commonly used polymer for microelectromechanical systems, and extensively applied as a biocompatible material for implanted structures [46].

The designed structure can be described as a LC circuit, where the equivalent lumped circuit elements (L and C) are arranged by the thickness, electrical properties of the dielectric substrate, width of conductor line, and conductivity of the deposited conductor layer. L is the inductance of entire rings and C is the total distributive capacitance between the layers. Due to broadside coupling, very large distributed capacitance was formed between the rings that can substantially reduce the electrical size of the structure compared to the resonance wavelength [47].

4.2.2 Marker Characterization

In order to characterize the MRI properties of our resonator structure, test resonator markers were fabricated to qualify the resonator characteristics. Therefore, the reflection coefficient (S_{11}) of the resonator, which is weakly coupled to pick-up coil, was measured using a network analyzer (Agilent E5061A, Santa Clara,

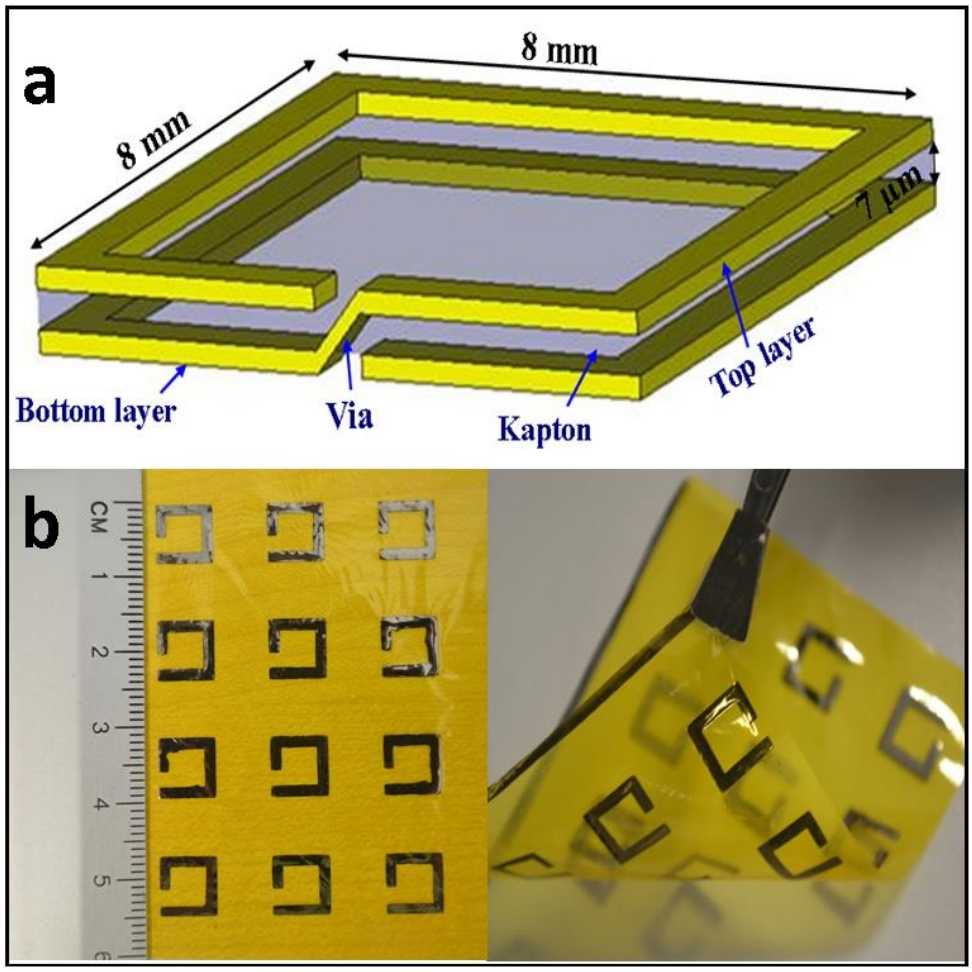

Figure 4.1: (**a**): 3D schematic of the architectural construction of our passive RF-resonator marker (not drown to scale). The device structure consists of two metal layer SRRs that are patterned on both sides of the Kapton dielectric substrate where layers are connected to each other through via metallization. (**b,c**): An array of 8 mm $\times$8 mm resonator markers that fabricated on a 7 μm-thick flexible Kapton film.

California). Characterizations for the ultimate device were achieved with the resonator marker and pick-up coil immersed in liquid saline phantom. The passive resonator marker was designed to work in the resonance frequency of 3T MR scanner (Siemens Magnetron Trio, Germany, f_0=123 MHz). The characteristic of passive RF resonator marker was evaluated using both full EM numerical simulation (CST Microwave Studio, Germany) and analytical methods. Simulation setup contained a resonator marker positioned perpendicular to static magnetic field (i.e., normal of planar resonator is perpendicular to B_0) that was located in the isocenter of cylindrical saline phantom (22 cm in diameter and 15 cm in height, dielectric constant: 70, conductivity: 0.65 S/m). Measurement was conducted for both the loaded and unloaded (free space) cases. In analytical method, the resistance ($R = 0.55\Omega$) and inductance (L=31 nH) values for the unloaded resonator marker tuned to 123 MHz were calculated.

The characteristics of the resonator marker were evaluated on both unloaded and loaded cases. Measured frequency responses of the resonator marker at the module of reflection coefficient showed that loading effect shifted down the resonance frequency. To compensate this frequency shift, the marker operating frequency was tuned to higher frequency in free space, which was shifted down to scanner Larmor frequency by loading effect.

4.2.2.1 Phantom MR Experiments

Image acquisition was performed using the 3T MR scanner on standard saline phantom. The phantom was excited by a body RF coil, where surrounding the phantom signal was collected by a 12-channel head coil (Siemens). MR images were acquired using gradient echo (GRE) sequences. According to these image groups, SNR analysis was performed to determine the signal homogeneity and penetration depth. The SNR profile was calculated by dividing averaged image signal intensity by standard deviation of noise. Sequence parameters for phantom experiment were: repetition time (TR) =300 ms, echo time (TE) =10 ms, matrix size = 256×256, slice thickness =3 mm, field-of-view (FOV) = 220×220 mm^2.

B_1^+ map was derived at the vicinity of the resonator marker to determine the B_1-filed distribution due to the resonator. Generally, the B_1^+ map at the proximity of the resonator marker consists of B_1-field of the transmit coil and magnetic field contribution from inductive coupling of resonator with B_1-field. The induced current on the resonator generates a linearly polarized magnetic field $B_R(t)$, which can be decomposed into right and left rotating polarized components.

$$B_R(t) = B_{RR}(t) + B_{RL}(t) \tag{4.1}$$

where $B_{RR}(t)$ and $B_{RL}(t)$ are right and left circularly polarized fields component, respectively. The excited spins in MRI generate a rotating magnetic field that can be picked up by a forward-polarized receive coil, therefore, only left circularly polarized field component, $B_{RL}(t)$, contributes to a B_1^+ map. Double FA B_1^+ map [48] (3T, spin-echo, TR/TE = 3000/12 ms, matrix size=256×256, slice thickness=2 mm) was obtained in the phantom included a resonator marker.

The transverse component of the magnetization that can be obtained with a spoiled GRE sequence is given by:

$$M_{ss} = M_0 \times \frac{(1-E)sin\alpha}{1 - Ecos\alpha} \tag{4.2}$$

where E=exp $\frac{-TR}{T1}$, M_0 is the equilibrium magnetization, and is background FA (the angle that defied by the operator). The phantom (saline, T_1=220 ms) signal intensity was systematically investigated for both with and without resonator marker cases as a function of the background FA. The maximum signal intensity for without marker case occurs when the background FA of about 76^o is excited ($\alpha_E = 76^o$ when TR=250 ms). Accordingly, maximum signal intensity for resonator case was expected to be obtained at $\alpha_{ER} = (\alpha_E/Q)^o$. Q is the quality factor of the resonator.

4.2.2.2 Orientation Dependency Experiments

The coupling of the RF transmit field and the resonator marker is directly related to the resonator orientation. The transmit field can be decomposed to perpendicular and transverse components to the surface normal vector of the resonator. Only transverse component will contribute in effective received signal. Therefore, to achieve the highest performance, the surface normal vector of the resonator marker must be aligned perpendicular to the static magnetic field. We quantitatively estimated the signal enhancement as a function of the orientation of the resonator normal axis with respect to the applied RF field axis. The resonator inside the phantom was aligned to different orientations with respect to magnetic RF field axis from 0^o to 90^o in steps of 5^o (the concept is same as steering the linearly-polarized transmit magnetic field (B_1) using transmit array system with respect to the resonator axis). The sensitivity of signal intensity on the resonator orientation with regards to the alignment of the main magnetic field was evaluated by estimating the mean signal intensity in the region of interest (ROI).

4.2.2.3 Accuracy Tests

Accuracy test was conducted using a commercial graded phantom. The resonator marker can be set at any (x,z) point inside the phantom. One resonator was placed at the isocenter, while the x and z directions of the phantom were properly aligned to the scanner axes. Another resonator was translated along the xz plane to determine the accuracy of resonator localization at various spatial resolutions (Figure 4.2). We used a GRE sequence (TR=300 ms, TE=10 ms, FA=10^o, slice thickness=3 mm, FOV =$220 \times 220\ mm^2$) to calculate the localization accuracy. The errors between the actual position of the resonator marker and the corresponding MRI determined location (x, z) were calculated as Euclidean distance.

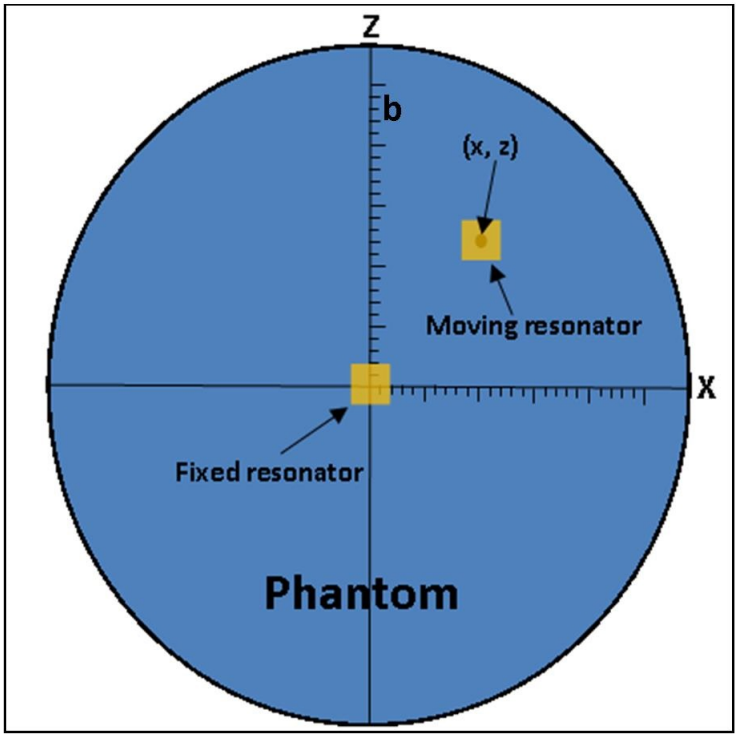

Figure 4.2: The xz plane schematic of the scaled phantom that is used for accuracy test. One resonator fixed at the center point and the other one interrogated on the xz plane. The localization error was reported as Euclidean distance.

4.2.2.4 RF Safety Tests

The proposed structure is not disable during transmit, so it may pose a hazard for the patient due to RF heating and associated temperature increases in tissue. Temperature analysis throughout the RF excitation was realized with our passive resonator marker tuned to the loaded resonance frequency. The resonator marker was immersed in cylindrical gel phantom with 40 cm in diameter and 25 cm height (heat resistivity=0.661 W/mK, heat conductivity=1.513 mK/W, heat capacity=4454 J/kg K, and diffusivity=1.48 mm^2/s). We used electromagnetic CST simulation to identify the possible highest specific absorption ratio (SAR) regions. Four fiber-optic lumens (P_1-P_4) of an optic thermometer (Neoptix, RF-04-1, Fiber optic temperature sensor, Canada) were set inside the phantom near the resonator which was predicted to show maximum heat. Fifth lumen, P_5 was used to collect the temperature at a reference point inside the phantom. The assembly was placed in the isocenter of the body coil [49]. The phantom with resonator inside was subjected under a high SAR sequence (GRE : TR=2.6 ms, TE=1.5 ms, FA=50^o, slice thickness=200 mm, slice number=2, FOV =220×220 mm^2, average=32). The sequence was continuously irradiated for 16 min at a field strength of 14 T, and then after by reaching stability the temperatures were acquired.

4.2.2.5 Marking in MR Experiments

Ex vivo animal experiments were performed on a head from an adult sheep cadaver. The aim of this experiment was to show the placement feasibility of our proposed passive resonator marker on cerebral cortex and in addition, to guide a biopsy needle to catch the targeted point inside the brain using proposed markers. For this purpose, an array of markers (4×5) was placed on the cerebral cortex of the cadaver. The cadaver head with the array of markers was positioned in a 3T MR scanner in head first spine. Imaging was realized by GRE sequence (TR=750 ms, TE=20 ms, matrix size=256×256, FA =15^o, slice thickness =3 mm, FOV =160×160 mm^2, bandwidth =260 Hz/Px) using the body coil as transmitter and

the 12-channel head coil as receiver. For the biopsy needle placement, transvers and sagittal MR images of the brain were obtained, where the intersection of the images lines represented the target point. The contrast of the marker with respect to morphological MR images allowed identifying the markers localizations at the brain surface.

Human experiments were performed on a volunteer in accordance with organization set approved by Yildirim Beyazit Hospital institutional review board (Ref:26379996/18, see Figure A.1). The wireless passive RF-based markers performance was studied on forehead and knee. For head scanning, the volunteer with aligned markers on the forehead was placed in head first position inside a 3T MR scanner where a body RF coil was used as transmitter and a 12-channel head coil as receiver. Knee was scanned using 15-channel transmit/receive coil (Siemens). The same imaging protocol as ex vivo experiments was applied for human imaging.

Clinical study of the proposed resonator markers was performed on a patient with a brain tumor in accordance with organization set approved by Yildirim Beyazit Hospital institutional review board (Ref:26379996/18, see Figure A.1) in Ataturk Hospital. After the patient was positioned on scanner table, an array of resonator markers (2×2) was fixed on the head of the patient. The position of resonator markers with respect to the mass was confirmed using T_1-weighted GRE acquisition (TR=750 ms, TE=20 ms, matrix size=256×256, FA =20^o, slice thickness =3 mm, FOV =$160 \times 160 mm^2$, bandwidth =260 Hz/Px). After image acquisition on the coronal and sagittal planes the patient table was withdrawn from the scanner. A target point for the biopsy needle insertion was selected and marked graphically on the head.

4.3 Results and Discussion

4.3.1 Effect of the Marker in the Phantom and Accuracy

Figure 4.3 reveals the feasibility of coronal and transverse imaging of the wireless resonator marker with corresponding SNR profiles. The marker is visible for ~ 4 mm depth penetration in transversal plane (Figure 4.3a) and ~ 8 mm $\times 8$ mm surface area in the coronal plane (Figure 4.3b). Inductive coupling between the resonator marker and surrounding medium leads to local signal enhancement at the vicinity of the marker. Consequently, a high-intensity signal is detected from the medium that is influenced by the marker. Strong sensitivity enhancement at the center of the marker is indicated by a sharp peak in the SNR profile of both the coronal and transverse images (Figures 3c, d). By moving away from the marker, SNR decrease is also more obvious in these profiles.

B_1 map analysis shows the spatial distribution of the RF magnetic field at the phantom included resonator marker (Figure 4.4). Field generated by the resonator results in FA amplification around the resonator, which by moving away from center of the resonator, this enhancement is diminished. Null B_1-field at some reigns around the resonator is due to the cancelation of the total B_1-field generated by excitation RF field and resonator filed that is shown by dark regions (Figure 4.3b). Maximum FA gain of ~ 2.3 was obtained at the close vicinity of the resonator.

With the passive resonator marker immersed in the saline phantom, imaging with low FA in the range of $6 - 18^o$ led to high signal intensity, consequently acceptable marker-to-background contrast. An excitation angle of 8^o presented the highest marker signal intensity (Figure 4.5a). Considering data plotted in Figure 5.5a, the maximum signal intensity was occurred at background FA of 82^o for without resonator case that is in good agreement with calculated Ernst angle ($\alpha_E = 76^o$). It can be observed that maximum signal at the proximity of the resonator already acquired when the background FA was in the range of 8^o, which corresponds to 82^o in without resonator case. The ratio of background

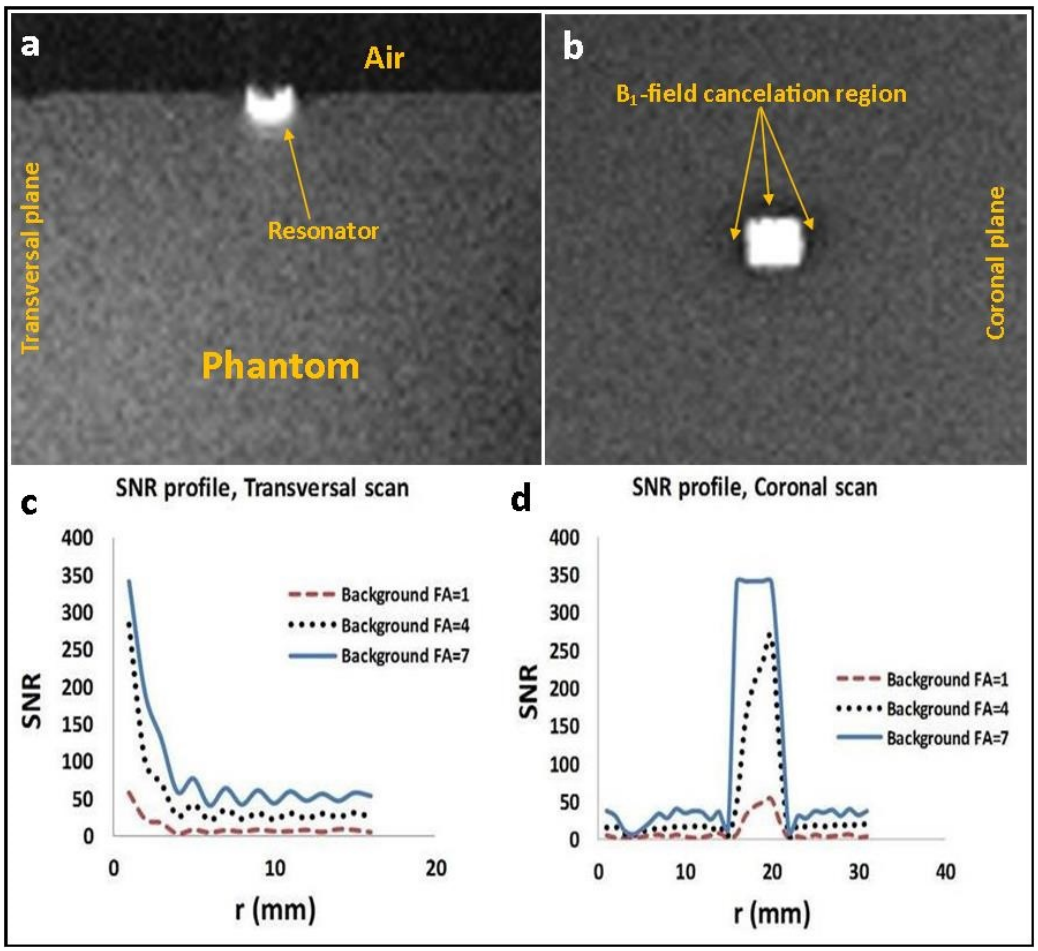

Figure 4.3: (**a,b**): Transversal and coronal low FA GRE images of a $8mm \times 8mm$ resonator markers. The markers are placed in the middle of saline phantom. Bright spot indicates the effect of marker in local signal amplification, which leads to high marker-to-background contrast at very low excitation angle. (**c,d**): Cross-section of SNR profile through the middle marker shown in transversal scan (a) and in coronal scan (b), respectively at three different background FAs. SNR is calculated as the ratio of image signal intensity to the standard deviation of noise.

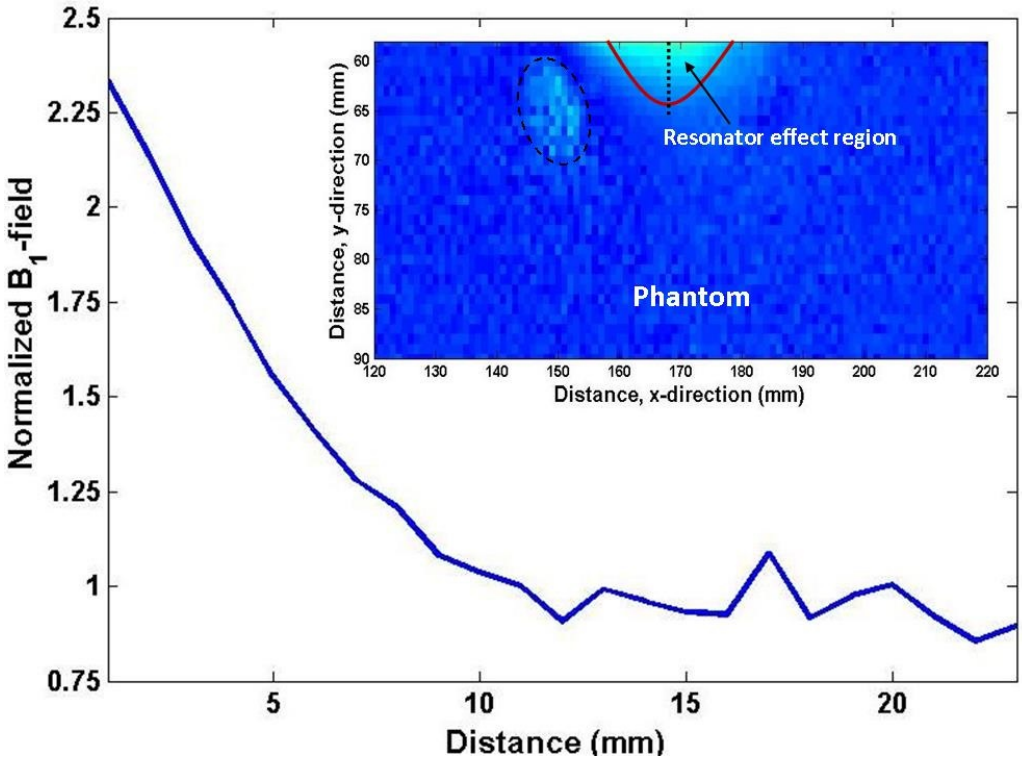

Figure 4.4: B_1-field distribution of a phantom with the resonator marker inside. Double angel method is used to analyze the B_1-field distribution and the effect of the resonator. Generated field by the resonator enhances the FA at its close proximity. Plotted FA profile (Normalized to background phantom (B_1) value) shows maximum FA amplification of 2.3. Depending on the applied power, resonator may disrupt the (B_1)-field at some points far from its vicinity (dashed ellipse). Straight dashed line indicates the (B_1)-profile path.

Table 4.1: Accuracy test results

Table 4.1: Accuracy test results							
Matrix size	Pixel size (mm)	$\mu_{\Delta x}$	$\mu_{\Delta y}$	μ_r	$\sigma_{\Delta x}$	$\sigma_{\Delta y}$	σ_r
64	3.44	0.69	0.78	0.73	0.37	0.45	0.36
128	1.72	0.54	0.66	0.60	0.31	0.40	0.32
256	0.88	0.40	0.53	0.46	0.26	0.37	0.27
384	0.57	0.28	0.41	0.34	0.17	0.25	0.22
512	0.43	0.19	0.28	0.23	0.14	0.19	0.15

FAs ($82^o/8^o \approx 10.2$) that resulted in maximum signal on both without and with resonator cases corresponds to the resonator Q-factor. Increasing background FAs results in a decrease of the resonator signal intensity at its vicinity.

Aligning the normal axis of the resonator marker perpendicular to the main magnetic field of the scanner presented the highest signal intensity, and consequently, the maximum SNR. Tilting the marker from the direction of the main magnetic field decreases the signal intensity (Figure 4.5b). As expected, the minimum signal intensity was obtained when the normal of the resonator marker was in the (B_0) direction. In this position the coupling between the resonator marker and the transmitter/receiver coils is minimized.

The accuracy test results of the resonator marker localization at different spatial resolutions are summarized in Table 4.1. These results indicate that the localization error measured along x and z axis at low special resolution is wider than at high resolution. Localization errors were calculated as a function of direction of the marker translation and spatial resolution.

4.3.2 RF Safety

CST simulation was performed to calculate the phantom SAR close to the resonator. The SAR gain of 1.41 was reported at the proximity of the resonator (Figure 4.6a). After estimating the maximum SAR regions, the temperature sensors were fixed on the related point around the resonator (Figure 4.6b). RF

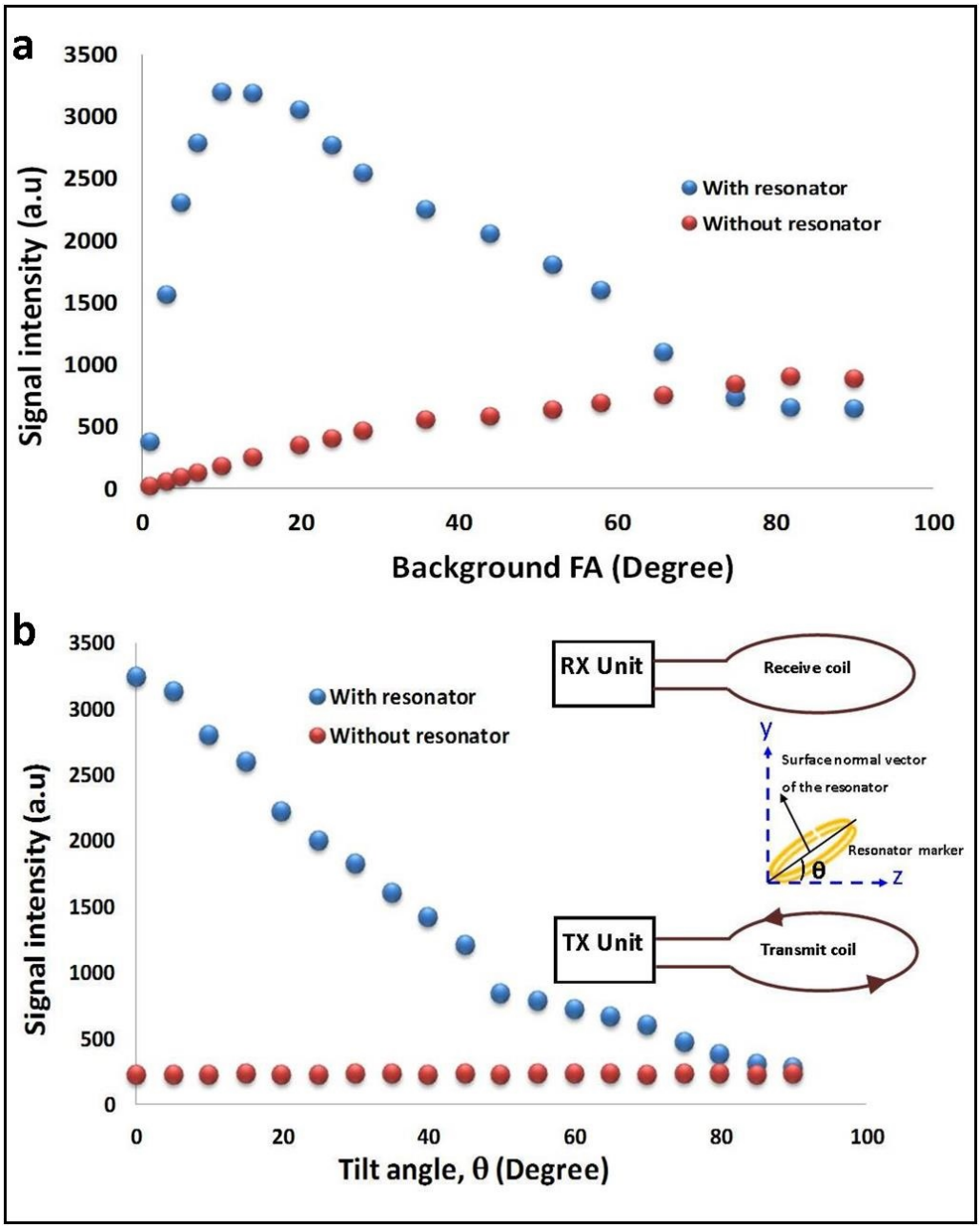

Figure 4.5: (**a**): Systematic evaluation of the phantom signals intensity with and without resonator as a function of the background FA. Resonator and phantom (without resonator) signals were collected in saline phantom with GRE imaging sequence. Here, the excitation angle of 8^o exhibits the highest marker signal intensity. Further increasing the FA decreases the marker signal and increases the background signal. (**b**): Coupling-dependence of signal intensity on the marker tilt angle (θ). With GRE pulse sequence the marker could be identified for a tilt angle up to 80^o.

heating measurements of the wireless resonator marker were safely performed under continuous high SAR MRI pulse GRE sequence. All the sensors were experienced close value of temperature raises ($P_1 = 2.1°C$, $P_2 = 1.7°C$, $P_3 = 1.8°C$, $P_4 = 1.7°C$ and $P_5 = 1.6°C$) (Figure 4.6c). The highest temperature raise of $2.1°C$ was measured at the point P_1. This can be explained by homogeneous electric field distribution of resonator within phantom, consequently less amount of hot spots. According to the simulation and experimental results, we reported the highest SAR gain of 1.62, which the calculated SAR is below the limits of U.S. food and drug administration (FDA). Marking based MRI experiments can also be accomplished with much lower RF field excitation. At this low power excitation, no heating was detected by any lumen.

4.3.3 Anatomical MRI

Figure 4.7 displays successful transverse (Figure 4.7b) and sagittal (Figure 4.7c) T_1-weighted marker visualization at 3T in cadaver cerebral cortex. Here, marker scanning performance on curved surfaces is also proved by these images. These passive resonator markers provided successful guiding of a biopsy needle inserted in cadaver brain. Figure 4.7a shows the photo of graphically marked resonators, set on cerebral cortex. The intersection of transvers and coronal planes indicates the insertion point to guide the needle to catch the assumptive target region that is surrounded by white ellipse in the image.

The results show that accurate and fast imaging capability of the resonator marker can provide excellent guidance modality for interventional instruments.

In the clinical study, the resonator markers fixed over the head of the patient provide robust localization signal that was shown as bright spots in the MR images with respect to the background anatomy (Figure 4.9a). The images were obtained on both coronal and sagittal planes. The position of tumor mass that is surrounded by white circle in Figure 4.9 is identified with respect to the resonators on these images. The intersection of two imaging planes represented a point to precisely insert biopsy needle (Figure 4.9b).

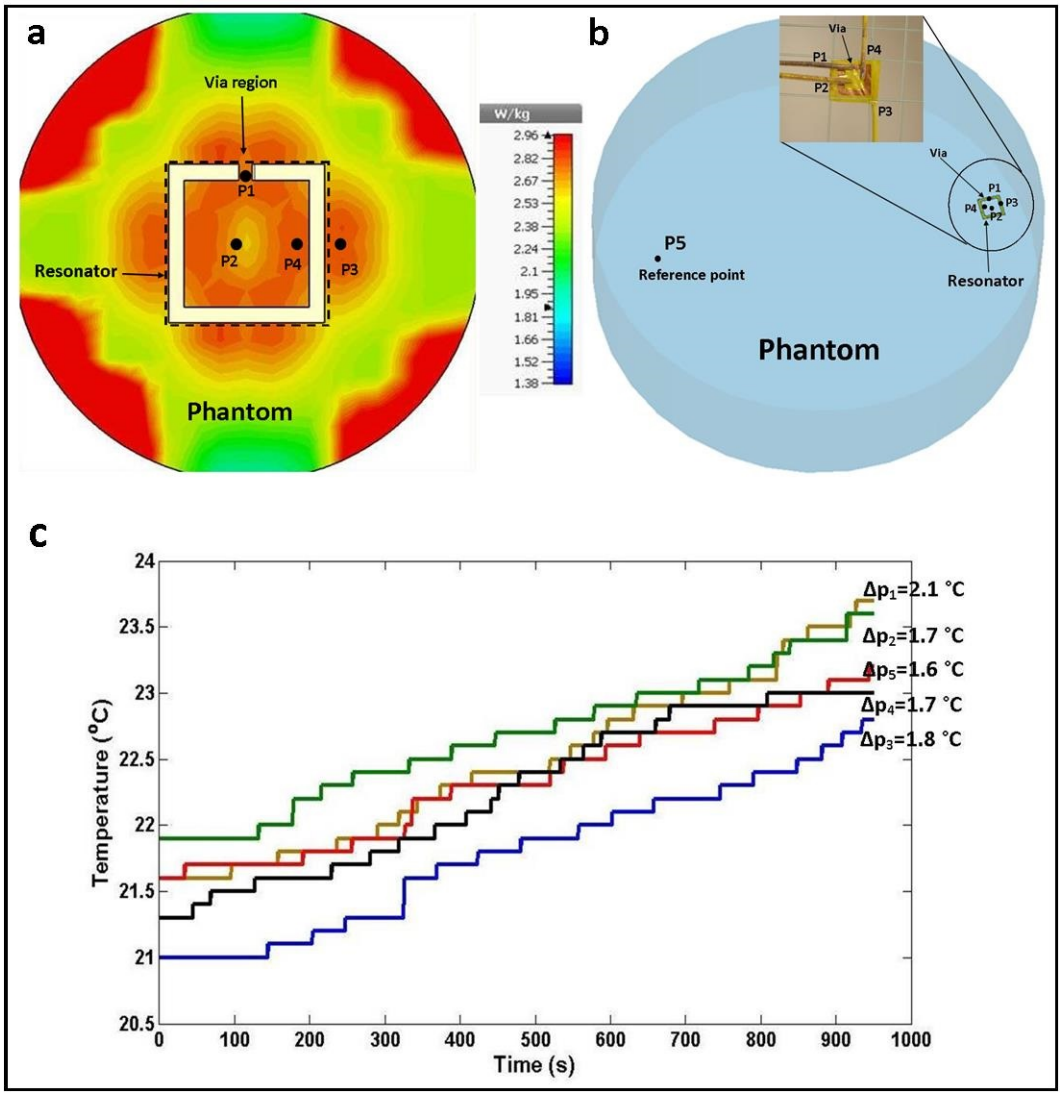

Figure 4.6: (**a**): Electromagnetic CST simulation is conducted to predict the highest heating places. P_1-P_5 indicate the location of temperature probes for heat measuring. (**b**): 3D schematic of the assembly to compute the local SAR. Photograph of the resonator with temperature sensors shows the arrangement of the lumens near the resonator. P_1 is placed near the via. P_2 is set close to center point, P_3 and P_4 are placed at the inner side and outer side of the resonator. P_5 is set at another corner of phantom, far of resonator marker as the reference sensor. (**c**):Temperature recording from probes P_1-P_5. Temperature raise during 16 min RF exposure at a continues high SAR pulse sequence. No significant temperature increases were reported over 16 min. Temperature data from reference point, P_5 shows $1.6°C$ increases. Maximum temperature raise is reported at P_1, $2.1°C$ that corresponds to SAR gain of 1.62.

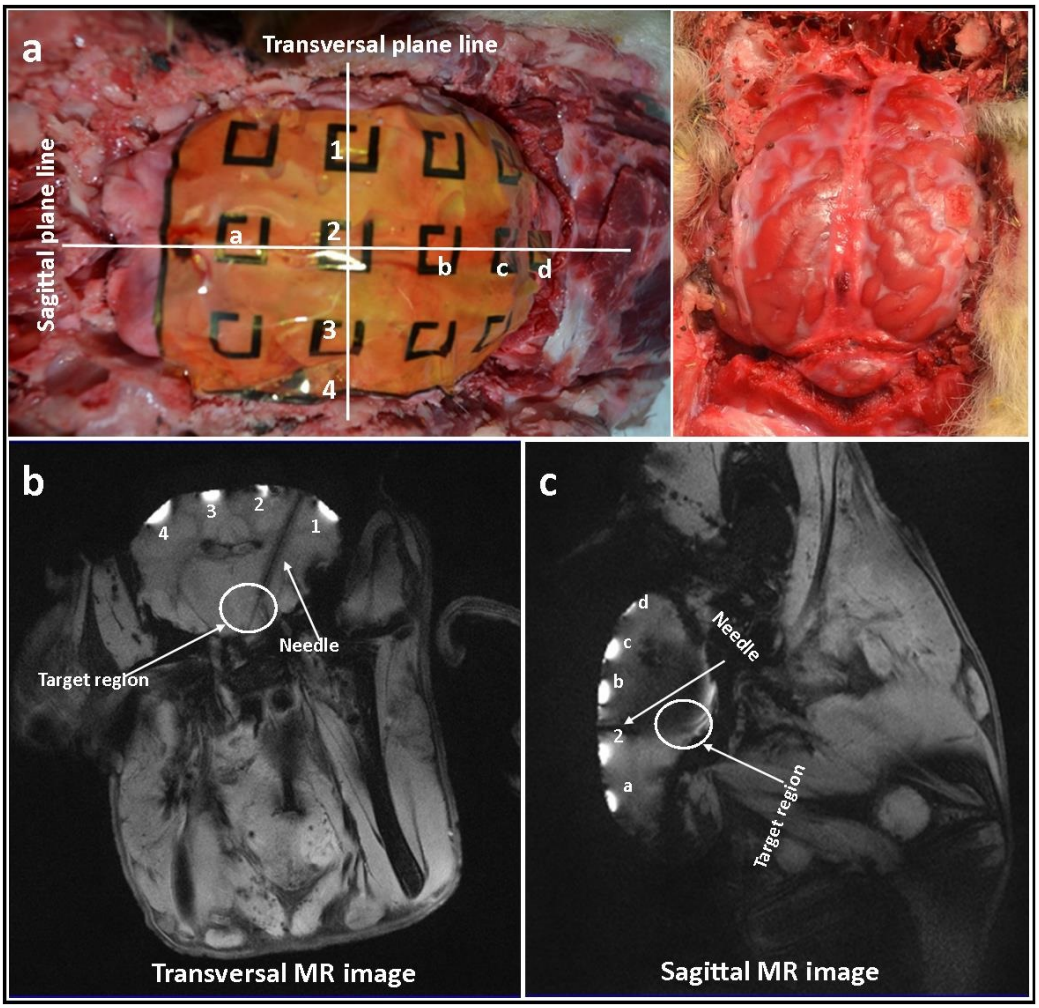

Figure 4.7: Ex-vivo marker study through the brain of a sheep. (**a**): An array of flexible markers was set on the cerebral cortex of the brain. Every marker is indicated by a code. Excitations in transversal and sagittal plans are shown by corresponding lines over the cerebral cortex. (**b,c**): Transversal and sagittal T_1-weighted GRE images of the array of markers over the brain along with an inserted non-magnetic needle was achieved. Each marker is denoted by its corresponding code in MR images. The position of needle with respect to the tissue and markers is clearly obvious.

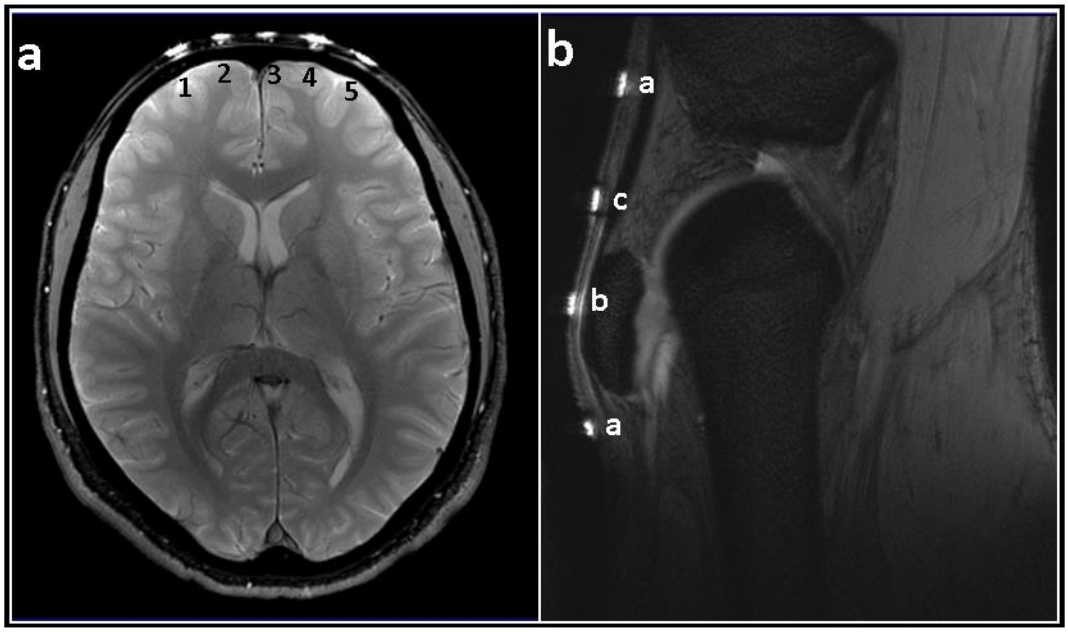

Figure 4.8: Anatomic tissue localization using our passive RF-resonator markers placed on human knee (**a**) and human head (**b**). Resulting GRE images, sagittal view of the knee and transversal view of the head provide useful information about the position of each marker with respect to the anatomic background.

4.4 Summary

In this part of the thesis, we demonstrated an ultra-thin, flexible, passive RF-based resonator marker that was successfully tested in clinic for marking purposes. The ultra-thin and flexible structure of our implemented device offers effective and safe MR visualization and improves the feasibility and reliability of anatomic marking and tracking at various surfaces of the body.

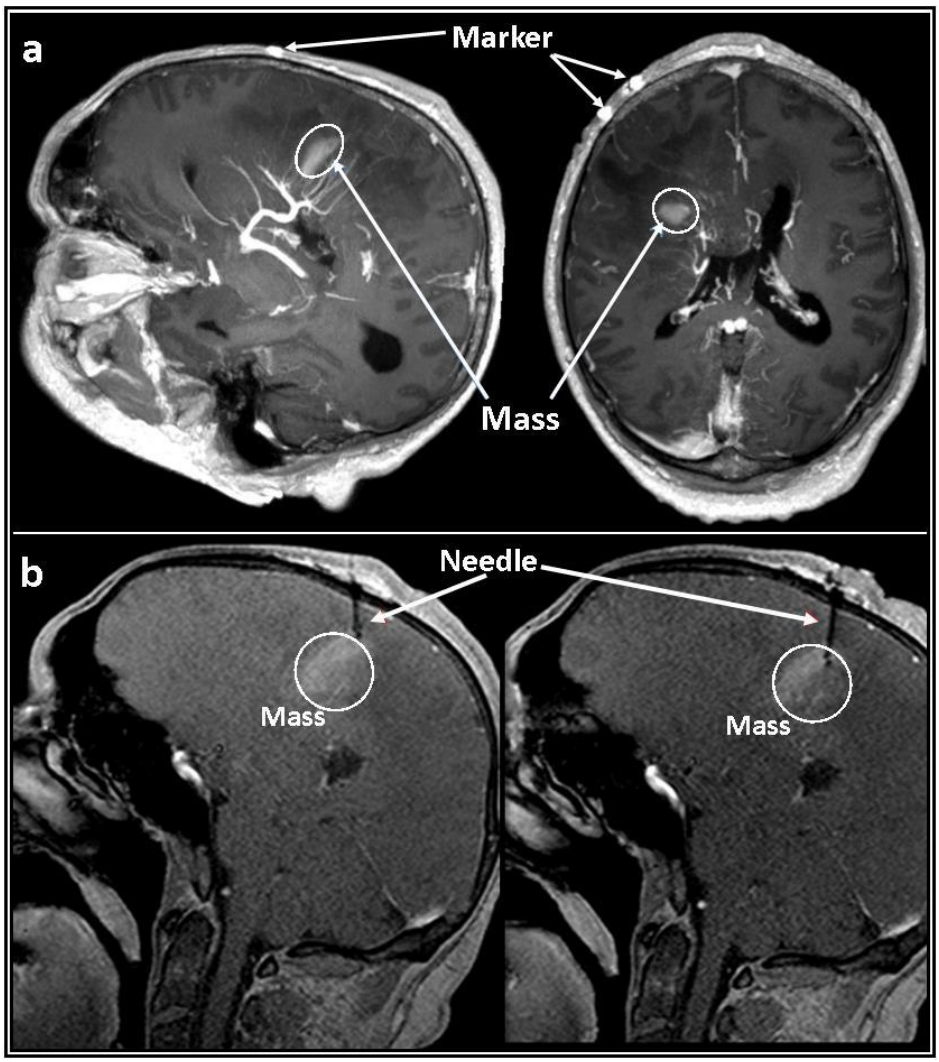

Figure 4.9: Clinical feasibility of biopsy needle guidance using resonator markers under 3T MRI scanner. An array of markers (2×2) was fixed on a patient head included a mass. (**a**): The position of the mass with respect to the markers is clearly indicated on T_1-weighted GRE images. (**b**): After graphically marking the positions of the markers and needle insertion point, the needle insertion procedure was conducted gradually. T_1-weighted GRE images show the position of the biopsy needle inside the brain close to the mass.

Chapter 5

Inductively Receive-Only Coupled Endoscopic Probing

This chapter is based on publication "An inductively receive-only passive resonator probe decoupled using linearly polarized excitation for endocavity MRI imaging "A.Alipour, V.Acikel, S.Gokyar, O.Algin, C.Oto, E.Atalar, and H.V.Demir, *under submission*.

5.1 Introduction

Endoscopy conducted using alternative imaging modalities including narrow-band imaging, magnifying endoscope, optical coherent tomography, autofluorescence endoscopy, and intravascular ultrasonography has been developed for observing suspect lesions in the gastrointestinal band and other body cavities as well as the guidance of minimally invasive interventions [50–54]. However, poor optical visibility at the depth and low tissue contrast limits the applications of these techniques. In addition, because of ultrasound signal diffraction or reduction in light scattering, the cancer stage cannot be diagnosed correctly using these modalities in some cases [55, 56].

MRI is widely used for visualizing soft tissues without radiation exposure. However, the image resolution of the localized area is limited with conventional external receive coils [57, 58]. To solve this problem, endocavity coils were proposed for imaging prostate, anal sphincter, and uterine cervix with improved image resolution in a localized region [39, 40]. Various techniques have also been developed for the MRI endocavity coil design. Active coils usually relay on either an antenna or small coils connected as separate receive channel [59, 60]. This method poses safety concerns due to long-wire connection and crosstalk. They can also limit the optical visualization, if the coils used in connection with an MR-compatible endoscope [61]. Another method is to use wireless passive RF coils, which is inductively coupled to a surface coil without wire connection to the MR scanner. However, this method is mostly used for tracking interventional devices [62–65].

Generated currents on a passive coil during RF excitation produce an oscillating magnetic field resulting in FA amplification and consequently B_1-field distortion at the proximity of the coil [66]. Strong coupling between RF excitation and passive coil can also bring about safety concerns [67]. The possible solution for this problem is decoupling the coil from the RF excitation field. Transmit array systems, which have recently been introduced for tracking position of the interventional devices [44], detecting the catheter rotational orientation [33], and reduction of implant heating [9], can be also used for decoupling purposes.

Here we introduce a method for performing MRI-endoscopy that employs a new class of an internal passive RF resonator probe in combination with dual-derived excitation to provide SNR-enhanced images of the localized region without disturbing the transmit B_1-field. We designed a thin and flexible passive RF resonator that is wrapped on a plastic tube with 7 mm in diameter. The proposed device is a broadside-coupled two-layer spiral resonator. The developed design used distributed inductor and capacitor to form an LC circuit to operate at the frequency of the 3T MR scanner.

The body birdcage coil of the Siemens scanner (Siemens Magnetron Trio, Germany, f_0=123 MHz) was used as transmit coil and head coil was used as receive

coil. Instead of conventional quadrature excitation of the birdcage coil, the two ports of the coil were driven in phase by weighting the voltage amplitudes at the ports to steer the direction of the LP B_1-field. To feed the two ports of the birdcage coil, 2 channels of an 8-channel transmit array system were used. Steering the LP B_1-field decoupled the resonator from the transmit field and left the resonator in receive coupling mode. This application resulted in the localized SNR enhancement at the proximity of the resonator probe without the transmit field profile distortion. In addition, transmit decoupling decreases the safety concern of tissue heating around the resonator.

We demonstrated and implemented these techniques in vitro at 3T MRI scanner, which exhibited SNR improvement, consequently resolution enhancement at the close proximity of the resonator as well as probe tracking. Also animal experiments were performed to show the in vivo applicability of the proposed method.

5.2 Method

In this study, the aim is to improve the SNR (or resolution) at the localized ROI at the endocavity region of the body using an interventional device. To avoid disturbing the B_1-field homogeneity and possible safety concern, the device is decoupled from transmit RF field during excitation using linearly-driven birdcage coil. To generate LP RF field, the birdcage coil was excited from both of its ports in phase instead of quadrature excitation. Weighting amplitudes of the excitations at the ports of the birdcage coil can steer the direction of the B_1-field.

A 3T MRI scanner was used in this study. Two ports of an eight-port transmit array system were used for RF excitation, and the 12-channel head coil (Siemens) and 15-channel knee coil (Siemens) were used for reception in phantom and in vivo experiments, respectively.

5.2.1 Probe Resonator

The proposed device is a broadside-coupled two-layer spiral resonator where the upper and lower layers are connected to each other through via metallization. The resonator is designed to operate at the resonance frequency of 3T MR scanner. Our design relies on the electrical parameters of the resonator, especially capacitance and inductance. The resonator was fabricated on a flexible substrate 35 μm thick polyimide film (Kapton HN, DuPont, Berlin, Germany). Thermal deposition method was used to pattern 15 μm thick gold layers on both sides of the Kapton substrate. The capacitor was included the Kapton film sandwiched between the two metal layers (figure 5.1a). The resonator has a parallelogram-shaped two-layer coil design with line lengths of 20 mm $\times$23 mm and a line width of 2.5 mm. Its metal thickness is 15 μm, which prevent the increase of the series resistance due to the skin effect (as the skin depth is 7.1 μm at 123 MHz). Flexible structure of the device allows for its twining simply on a 7-mm plastic tube. Finally, the bent resonator was coated with 200 μm-thick polydimethyl siloxane (PDMS) layer (figure 5.1b). PDMS (Dow Corning Sylgard 184 Silicone Elastomer, sigma-Aldrich, Germany) is a commonly used polymer especially for microelectromechanical systems, which is extensively applied as a biocompatible material for implanted structures. PDMS provides electrical isolation and biocompatibility and also decreases the capacitive effect between the resonator and the surrounding medium [46].

5.2.2 Probe Characterization

The device should be tuned to operate at the frequency of the 3T MRI scanner, 123 MHz. The resonance frequency of the resonator shifts down by the loading effect. Before the MRI experiment, the resonator probe was immersed in saline phantom (with conductivity of $\sigma = 0.7$ S/m and dielectric constant of $\epsilon_r = 80$) and tuned with a pick-up coil connected to a network analyzer (Agilent E5061A, Santa Clara, California). Due to the layer of PDMS on the resonator, operating frequency was less effected from the surrounding medium. The tuned resonance

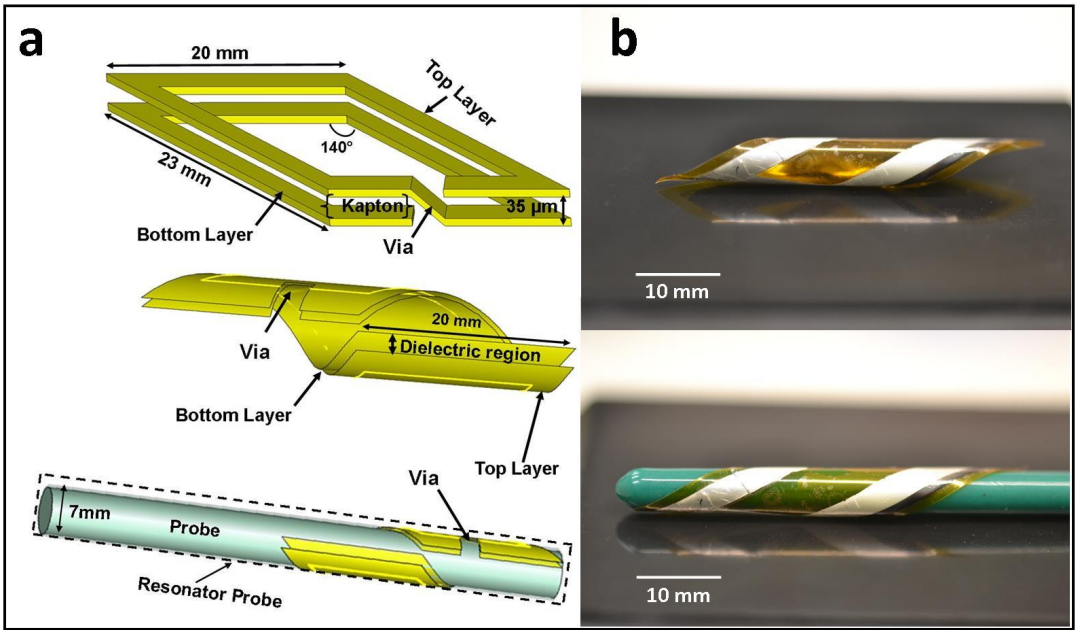

Figure 5.1: (**a**) Schematic of the proposed flexible passive parallelogram RF resonator probe, which consists of two metal layers with a dielectric film (Kapton) sandwiched between metal layers. The metal layers are physically connected by via metallization. The resonator was wrapped on a 7-mm plastic tube. (**b**) Photograph of our proposed passive endocavity resonator (top) and wrapped on a probe (down) used in an MR imaging procedure. To ensure the device biocompatibility, the probe was coated in its entirety with a thin layer of PDMS. This also facilitates the motion of probe inside body (rectum or esophagus).

frequency in phantom tends to change when the probe is sited inside the body, because the tissue loading is different from the loading in phantom. Variable device placement limited us in an exact and quantitative estimation of the shifting values. Therefore, the operating frequency of the bent resonator was tuned roughly to the value experimentally predicted in the saline phantom. The resonance frequency of the resonator was then adjusted by controlling the overlap region between the metal layers. Altering the overlap region changes the distributive capacitance and inductance values of the resonator, which results in the resonance frequency control.

5.2.2.1 MRI Performance

The phantom experiments were conducted by a 3T MRI scanner. The two ports of an eight-port transmit array system body coil was used for transmission and a 12-channel head coil was connected for reception. MR shimming was realized for all imaging protocols using the embedded scanners process based on the phase array coil signal.

Adjusting the amplitudes of the transmit array system ports steered the LP magnetic field orientation with respect to the resonator probe, consequently changed the coupling value. MR signals were collected at various coupling values. SNR profile was calculated to determine the signal variations at different coupling levels (θ). SNR analysis was conducted using the same pulse sequences for the MR signal and the separately obtained noise images. Gradient echo (GRE) sequences (TE/TR = 12/565 ms, FA = 10^o, slice thickness = 4 mm, matrix size = 256×256, field of view (FOV) = 134×134 mm^2, average = 32) were used to obtain both MR and noise signals. SNR is computed as follows [68]:

$$SNR = \frac{S_{avr}}{\sqrt{2N({\sigma_n}^2 + {m_n}^2)}} \tag{5.1}$$

where S_{avr} is the averaged signal intensity, and σ_n and m_n are the standard deviation and mean value of noise, respectively.

The 0.35 % saline resolution phantom was constructed of a quartz cylindrical container (22 cm in diameter and 15 cm in height) containing 150 μm micro-bars that are separated by 300 μm gaps. The combination of a resonator probe and micro-bars in solution was used as a sample to demonstrate the resolution and sensitivity. The resonator probe was placed by 2 mm space on top of the bar phantom. High-resolution MR images with/without resonator were obtained using a GRE sequence with TR/TE = 9/300 ms, FA = 10^o, slice thickness =3 mm, matrix size = 256×256, and FOV = 60×60 mm^2.

B_1^+ map analyses were used to show the effect of the coupled resonator on the B_1^+-field distribution inside phantom. The phantom contained of 2.5 L saline solution with a conductivity of 0.6 S/m. When the excitation RF field is coupled with the device, B_1^+ map at the vicinity of the resonator consists of magnetic field contributions of the induced current in resonator and from the transmit coil field, but no contribution from the resonator when they are decoupled. To estimate the resonator contribution, B_1^+ map procedure was conducted for both strongly coupled and decoupled conditions. Double flip angle [48] B_1^+ maps (GRE, TR/TE = 1000/10 ms, matrix size = 256×256, FOV = 140×140 mm^2) were obtained at axial slices along the resonator.

The proposed structure is decoupled during RF transmit, so it minimizes the possible safety hazard of heating. But for the worst case scenario, RF safety was tested when the device was coupled with the RF excitation. Heating test was conducted with the resonator probe inside a cylindrical phantom (25 cm in height and 40 cm in diameter) prepared with 30 gL^{-1} polyacrylic acid to protect convection. A high SAR GRE pulse sequence (TR = 2.6 ms, TE = 1.5 ms, FA = 50^o, slice thickness = 200 mm, slice number = 2, FOV=410×410 mm^2, average = 32) was applied continuously to the assembly for 20 min. The possible high SAR points were indicated using simulation (CST Microwave Studio) results. E-field distribution is shown in the axial (Figure 5.2a) and transversal (Figure 5.2b) planes around the resonator. The temperature sensors were fixed at the areas with high electric field confinement. Temperature was monitored with fiber-optic temperature sensors of an optic thermometer (Neoptix RF-04-1 fiber optic temperature sensor, Canada). Sensors P_1-P_4 were set around the resonator and the

sensor P_5 was positioned at a point far away the resonator as the reference point (Figure 5.2c). The resonator probe was placed at the most off-center position where it experienced a high SAR value.

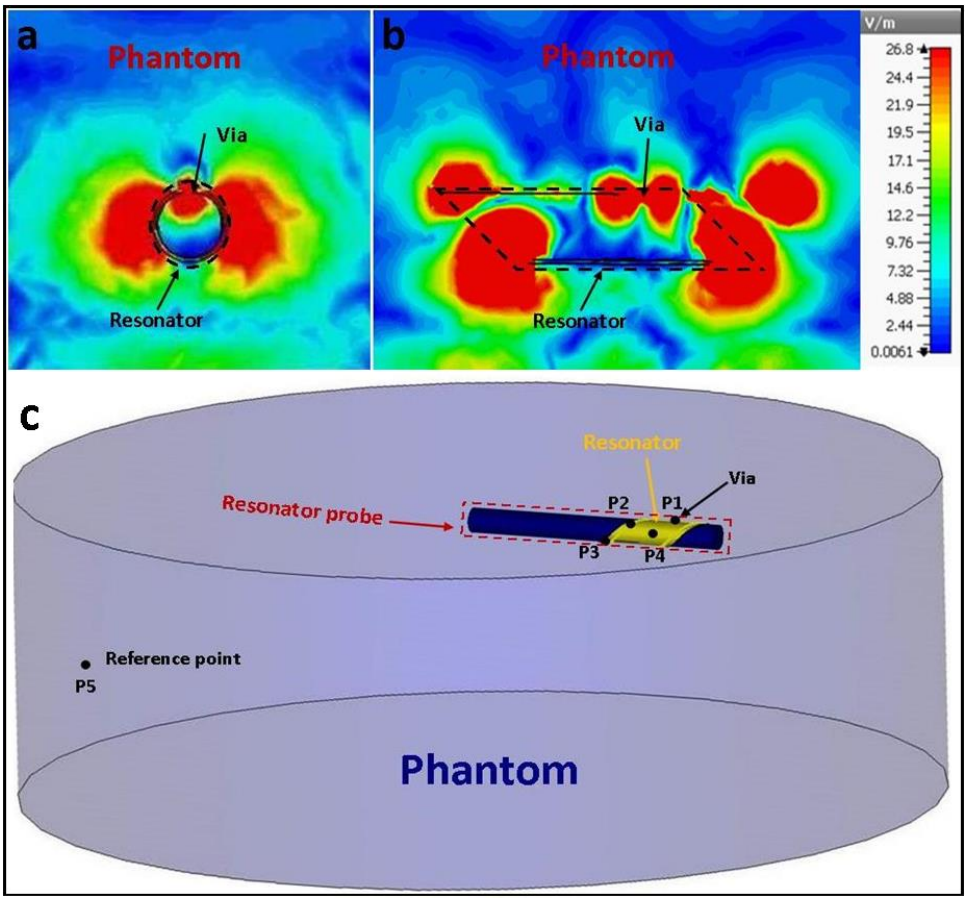

Figure 5.2: CST simulation results are used to identify the possible high SAR regions around the resonator. Axial (**a**) and transversal (**b**) planes of the electric field distribution around the coupled resonator. Regions with high electric field values are expected to have high value of SAR. **c**: Schematic of the resonator probe inside the cylindrical phantom and photograph of the resonator with fixed temperature sensors around. Black dots (P_1-P_5) show the position of the temperature sensors that are fixed around the resonator.

5.2.2.2 In Vivo Experiments

Animal experiments were approved by Bilkent University Institute of Animal Care Committee and performed by the national standards of animal care (Ref:2014/38,

Table 5.1: In vivo MRI imaging protocol.

Table 5.1: In vivo MRI imaging protocol.		
Sequence/Parameters	T1-GRE	T2-GRE
TR/TE	520/4.18 ms	992/46 ms
Slice thickness	3 mm	3 mm
FOV	120×120	120×120
Acquisition time	3.5 min	4.5 min
FA	25^o	25^o
Matrix size	384×384	256×256

see Figure A.2). A New Zealand rabbit (2.8 kg) was obtained from Ankara University Animal Laboratory and were maintained in standard laboratory conditions. In vivo MR imaging experiments were performed with 3T MRI scanner. The animal was subjected under general anesthesia before intubation. For premedication, 1 mg/kg Atropine was injected intramuscularly before anesthesia. The anesthesia was inducted using an intramuscular injection of Xylazine (10 mg/kg) and Ketamin (30 mg/kg).

Sterilized passive endocavity resonator probe traveled through the rectum of the under anesthesia rabbit. Rabbit was scanned in a prone position without preimaging preparation using 3T MR scanner. The linearly driven birdcage body coil was used for RF transmission and the 15-channel knee coil was used for signal reception. Anatomical structure imaging was conducted with T_2^*-weighted GRE sequences. Sequence parameters and details of the MRI protocol are presented in Table 5.1.

5.3 Results and Discussion

5.3.1 Phantom Experiments

Figure 5.3 shows the SNR profiles of the resonator probe and background phantom at different coupling levels, (θ). In each sequence, the applied LP magnetic field was rotated by approximately 5^o. The experiment was made for a rotation range

of $\theta = 5^o$ to $\theta = 150^o$. This profile indicates that the maximum SNR is obtained at $\theta = 90^o$, where the LP RF transmit field sits perpendicular on the resonator probe axis (along z-axis). As expected, the resonator is decoupled from the transmit RF field when the applied RF field is aligned parallel to z-axis, corresponding to $\theta = 0^o$. The SNR at various coupling values shows that the background signal is independent of the orientation of the transmit RF field.

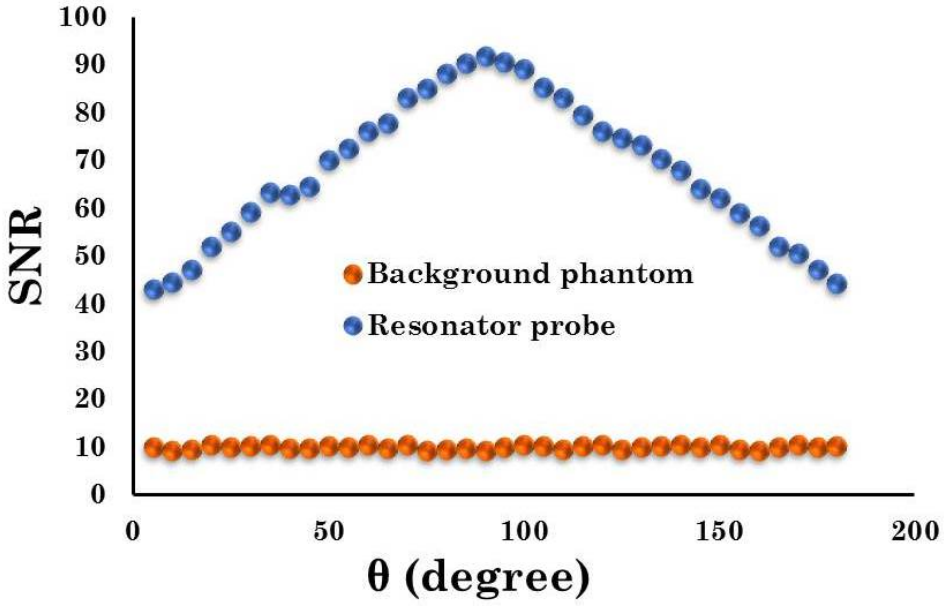

Figure 5.3: SNR profile of the resonator and background phantom versus orientation of the LP excitation (θ). The background phantom for all excitations angles shows almost the same signal values. The coupling value between the excitation field and resonator changes by θ. At $\theta = 0^o$ and $\theta = 180^o$, the resonator is decoupled from the LP transmit field. The signal difference between the resonator and the background shows that the signal enhancement occurs only in the reception mode when the resonator is decoupled.

The resolution test was carried out with the resonator probe that was placed with a 2 mm separation on top of the micro-bars inside the resolution phantom (Figure 5.4a). MR images for both with and without the resonator were obtained using GRE sequences for the resonator decoupled position (Figures 5.4b,c). SNR enhancement at the proximity of the resonator probe resulted in the better visibility of the micro-bars, which were not resolved without resonator.

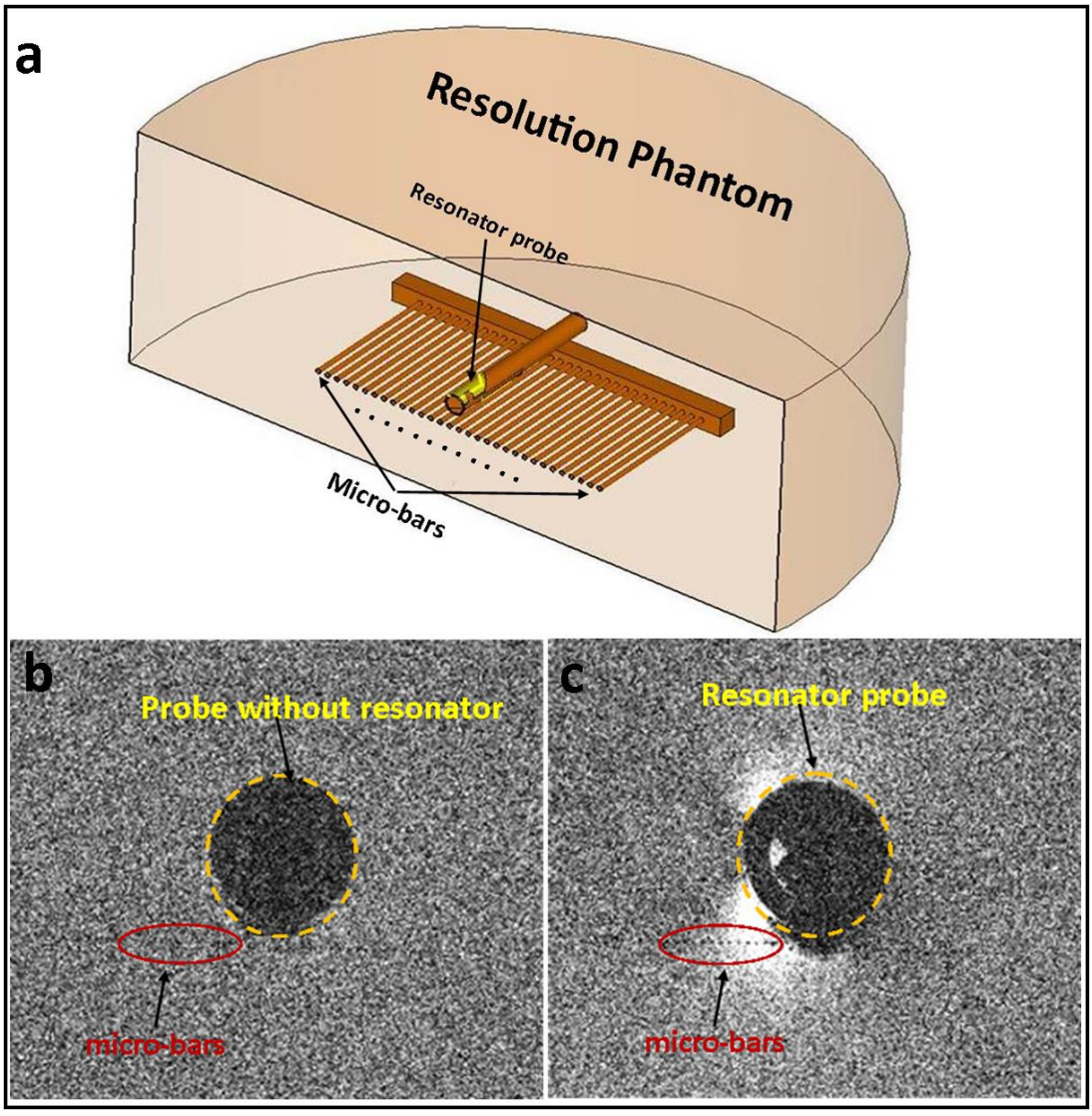

Figure 5.4: **a**: Schematic of the resolution phantom. The resonator probe was set on the resolution phantom (including fibers with 200 μm in diameter). Coronal MR images obtained using resolution phantom for without (**b**) and with (**c**) decoupled resonator. Due to low SNR around the probe, it is difficult to distinguish the micro-bars without the resonator. Local SNR enhancement at the vicinity of the resonator allows for the visibility of the bars in the presence of the resonator. Imaging was conducted in the decoupled mode.

Figure 5.5 contains B_1^+ maps and corresponding gain profiles from the phantom experiment around the resonator probe for both the coupled and decoupled positions. Resonator in the coupled case disturbs the B_1^+-field homogeneity at the proximity of the resonator. The gain profile along the dashed line shows the maximum B_1 amplification of about 3.5 at the vicinity of the resonator. When the resonator is decoupled from the transmit field, there is no identifiable distortion in the B_1^+-field (Figure 5.5). Negligible B_1-field distortion around the resonator can be explained by slight transmit coupling effect.

The heating test in coupled position under high SAR experiment conditions shows that all the sensors (P_1-P_4) fixed at the proximity of the resonator report approximately the same amount of heating ($P_1 = 2.2°C$, $P_2 = 2.1°C$, $P_3 = 2.0°C$, $P_4 = 2.0°C$) while reference point P_5 recorded $1.7°C$ temperature increase (Figure 5.6) . In the worse-case scenario, the highest SAR gain of 1.54 was reported which is lower than the FDA limits.

In the case that the resonator is decoupled from the transmit RF field, no current will induce on the device and also intrinsically the E-field will be vanished at the same plane. Therefore, a negligible amount of SAR gain is expected for the decoupled mode.

5.3.2 In Vivo Imaging

T_2^*-and T_1-weighted images, obtained with transmit-decoupled passive resonator probe positioned in rectum, allowed prominent SNR enhancement at the rectum wall structure at the close proximity of the resonator (Figures 5.7, 8). Multiple slices were acquired in transversal and sagittal planes. In these images the resonator probe can be clearly distinguished from morphological tissue. These procedures were used to evaluate the performance of the resonator probe as a proof-of-concept in vivo imaging at the rectum. The sequence parameters were selected as a compromise between high special resolution and small artifact size.

After the experiment was over, the general condition of the animal was good

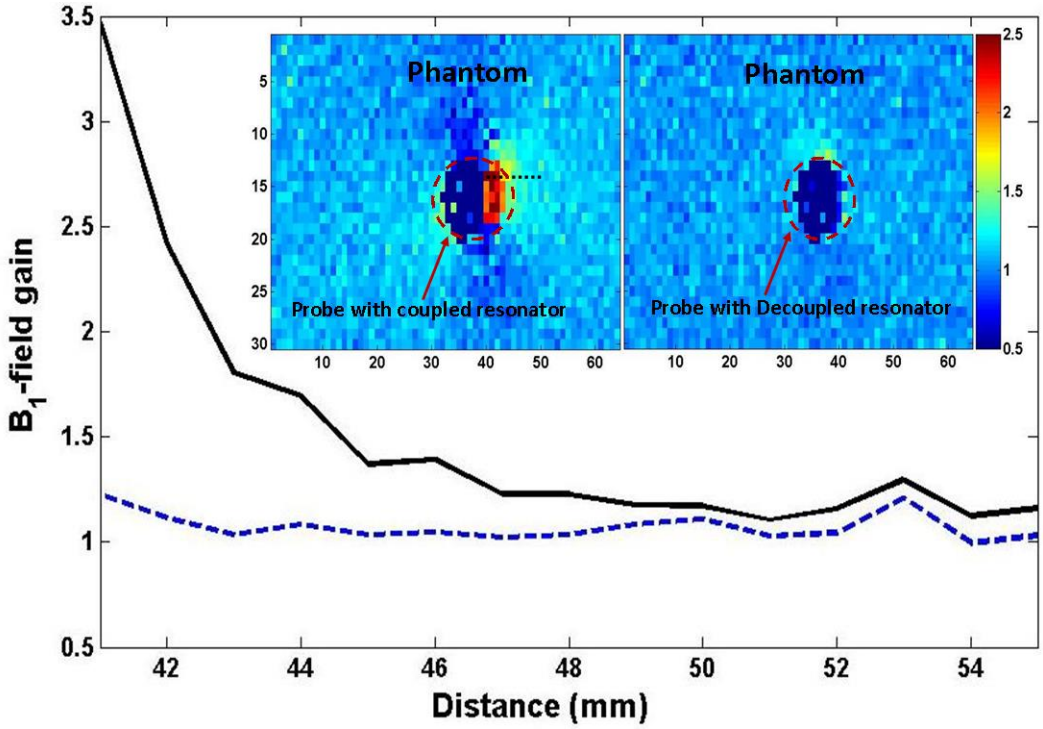

Figure 5.5: Double angle B_1^+ maps show the B_1^+-field distribution around the resonator inside phantom in the coupled and decoupled positions. For the coupled mode, induced current on the resonator creates a magnetic field that disturbs the B_1^+-field homogeneity (amplified the FA at its close proximity). Transmit RF decoupling prevents additional magnetic field around the resonator, consequently leading to no B_1^+-field distortion.

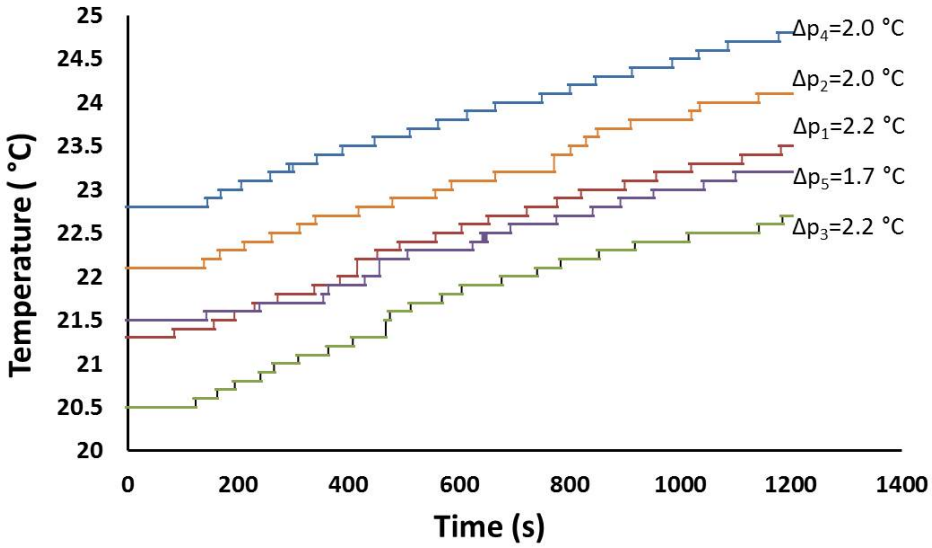

Figure 5.6: Heating test was performed using high SAR sequences when the resonator was in the coupled position. Four temperature sensors were positioned at different points around the resonator and one sensor collected the temperature data at a point far away from resonator (reference point). Temperature increases linearly at all the points, the maximum temperature raise is recorded at P_1 and the highest SAR gain of 1.54 is calculated.

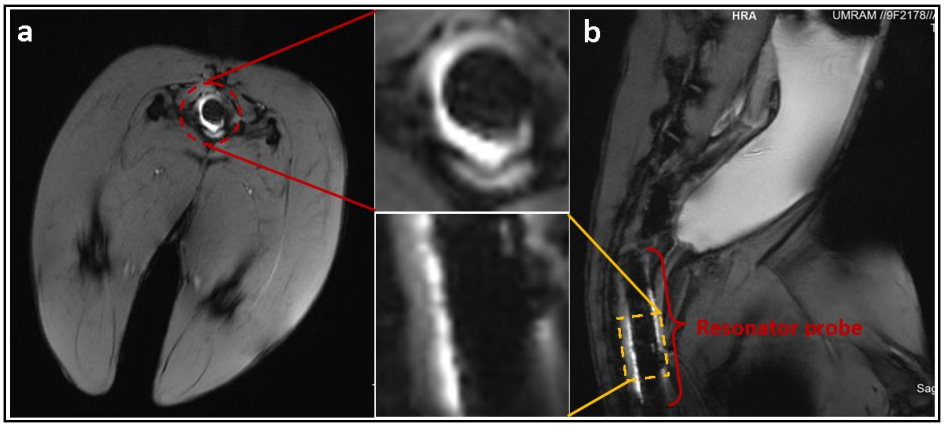

Figure 5.7: Normal rabbit rectum anatomy with resonator probe inside: imaging was performed using the decoupled mode. The interventional device was coupled only with receive coil. Transversal (**a**) and sagittal (**b**) T_2^*-weighted GRE images (TR/TE=992/38 ms) of the rectum with the resonator probe and corresponding zoom-in images showing signal enhancement near the resonator that may improve the small features visibility.

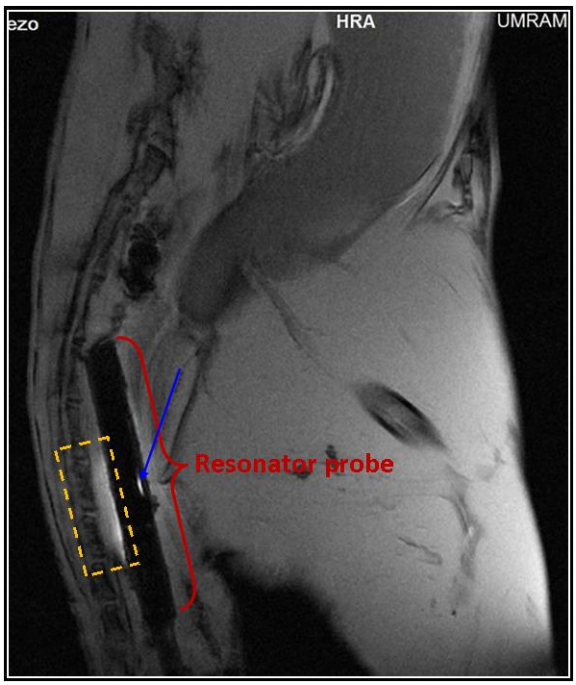

Figure 5.8: T_1-weighted GRE image (TR/TE=520/4.18 ms) of the rabbit rectum with the resonator probe inside. The probe is clearly visible inside the body. Yellow box shows the device effected region with SNR improvement in the vicinity of the resonator. Low signal enhancement can be explained by receive only coupled mode. The bright signal (shown by arrow) may originate from the liquid leakage under the resonator.

and no deformities were found in the resonators. Also, no complication was observed on rabbit during the MR imaging or in the clinical examination performed after the experiment.

5.4 Summary

In this chapter of the thesis, we presented a localized MR endocavity imaging technique that relies on LP excitation together in conjunction with a passive RF resonator probe structure. The proposed device is a flexible passive resonator using distributive elements to operate in a 3T MR scanner. Transmit coupling between RF excitation and passive resonator resulted in safety concerns and B_1-field inhomogeneity. Using a linearly driven birdcage coil, the device was decoupled from the LP excitation field, therefore resulting in minimized safety problem and preventing B_1-field inhomogeneity. Transmit decoupling left the resonator probe only in reception amplification position; consequently, SNR or resolution enhancement occurred in the vicinity of the resonator without B_1-field distortion.

Chapter 6

Conclusion

In this chapter, we provide a summary of the thesis work, present the conclusions and discuses the future outlook. The thesis basically comprises of three applications of thin-film microwave resonators that are all microfabricated to meet the specific requirements of their targeted application. These are wireless sensing and marking, with the latter one having two operating regimes of inductively coupled and uncoupled modes. Bellow we discuss each of them one by one.

The first part of the thesis work focuses on a new telemetric measurement technique and a passive RF sensor for distance-independent wireless strain monitoring. Here, distance-independent strain monitoring is achieved by measuring the impedance of the sensor in addition to its resonance. In our proposed telemetric monitoring, we include the impedance parameters of all electrical components to measure precisely the resonance frequency of the sensor. The proposed sensor consists of an ultra-thin and multilayer (metal-dielectric-metal) structure with comb-shaped SRRs that are patterned on both sides of the flexible dielectric. Top and bottom layers of the sensor are 90^o rotated with respect to each other. The specific architecture of this design allows for the both metal layers to contribute in the sensor electrical characteristics (f_0, Q-factor, and Z_s). The sensor is tested under various strain levels and at different interrogation distances. A linear relation between f_0 and $|Z_s|$ is obtained at different levels of strain. The

slope of this response gives the strain. This strong linearity results in excellent strain sensing performance. By taking the advantages of this telemetric measurement technique and sensor structure, distance-independent strain extraction has been successfully demonstrated as an important outcome of this thesis. The experimental findings of the thesis show that the sensor has excellent accuracy with less than 0.5 % error, and also exhibit great stability and reliability.

Our future study for wireless sensing will focus on the application areas of this strain sensor. The proposed sensor has great potential for performing faithful wireless strain measurement in vivo while the patient's body parts may be moving. This can be used to register strain variation precisely during bone fracture healing even when the patient fracture site can not be precisely located externally. Furthermore, future research needs to be conducted to improve sensing performance at longer interrogation distances, for example, using a power amplifier at the pick-up reader antenna side. These findings given for telemetric strain monitoring may be a promising method for the systems with varying interrogation distance. Although previous studies performed using passive wireless monitoring showed so far that changing the interrogation distance results in inaccurate measurement, the proposed approach in this thesis successfully resolves the problem of interrogation distance variation.

In the second part of this thesis, we demonstrated the clinical applications of our developed MR-visible passive RF-based resonator marker that was fabricated using standard microfabrication technique. Au metallization was performed on both sides of the flexible dielectric substrate. The sandwiched dielectric between two conductive layers ensured distributive capacitance between these layers. This capacitive region is the main parameter in resonance frequency tuning. The applied methodology consists of a passive RF resonator circuit that is inductively coupled to the RF receiver coils to eliminate any necessities for external sources. The proposed MR-visible structure introduced an ultra-thin, flexible, and passive resonator marker with various inherent benefits. Our device based on a self-resonating structure used distributed components (inductor and capacitor) to operate at Larmor frequency to provide more feasibility and reliable visualization at different surfaces of the body.

In the thesis, the B_1 map analysis of our resonator in MRI revealed a predominant contribution of the resonator marker in effective FA amplification. In operation the resonator increases the effective FA consequently leads to the local signal enhancement in the proximity of the marker at small background FAs ($6^o - 18^o$). The phantom signal variation for both the cases without and with the resonator is determined by altering the background FA. At small FAs the resonator signal is more dominant. Increasing the FA ensures simultaneous resonator and surrounding medium visualization.

One of the significant safety concerns in the use of our resonator marker is the possibility of local heating hazards due to inductive coupling during RF excitation. The proposed passive RF resonator structure uses distributed components, which result in less power dissipation in comparison with lumped elements. Furthermore, homogeneous electric field distribution of the resonator results in a small number of hot spots, consequently a small amount of heating at the vicinity of the resonator. The highest reported SAR value at the proximity of the resonator inside phantom is lower than the FDA limits. An additional advantage of this resonator marker is its weaker orientation dependency. This device displays maximum signal sensitivity when its surface normal vector is perpendicular to the static magnetic field. This is a necessary condition to achieve maximum signal intensity via coupling to RF coils. However, the marker leads to strong coupling efficiency even in the case misalignment with respect to its normal axis.

In the thesis ex vivo MR experiment on cadaver demonstrated the guidance of a needle using intersection of the coronal and sagittal planes in MRI images. Clinical feasibility and reliability of the resonator marker was also demonstrated to guide the biopsy needle. A patient with a tumour in brain was subjected under MR experiment to mark its position with respect to the background and markers. The approximate insertion point of the needle was estimated using intersection of the markers included coronal and sagittal planes in MRI images by a medical doctor expert in MRI-assisted operation. These ex vivo and human experiments show the standard clinical performance of these markers. The experimental results indicate that this resonator can be utilized for tissue-marking purposes in MRI at various body surfaces.

MR-interventional catheter systems tracking using modified version of these types of RF passive resonators remains as an important future work. This is intended to be used for determining the correct position of the intervention devices inside the body. For example, an ultra-thin, flexible, passive RF-based resonator marker was successfully tested in clinic for marking purposes. The ultra-thin and flexible variant of our implemented device offers effective and safe MR visualization and improves the feasibility and reliability of anatomic marking and tracking at various surfaces of the body. This technique may incite novel approaches in interventional MR-guided devices.

In the last part of the thesis, we focus on the SNR enhancement at any localized endocavity region of interest using transmit decoupled passive RF resonator. Endocavity interventional devices are necessary to obtain high resolution images of the localized region of interest when performing MRI-endoscopy. Such MRI endocavity RF devices are of two main types; they are either active or passive. As active devices use elongated wires to connect to the scanner, this method provides satisfactory high contrast images of tissue but causes safety hazards. On the other hand, the passive techniques use inductively-coupled RF coils without using a connection wire and the performance of the device depends on the orientation of the coil and the power of the applied pulse. The RF transmit and receive coupling is the main reason of the signal enhancement in the passive technique. Commercial circularly-polarized excitation can be replaced with LP excitation to cancel the transmit coupling and leave the resonator only in receive-coupled mode. This approach is the main demonstration made in this part of the thesis work as another important outcome of the thesis.

Here, we show a thin and flexible passive RF resonator probe for performing MRI-endoscopy to improve imaging performance of the ROI. The device benefits distributed components (L and C) to resonate at the operating frequency. Its flexibility allows for operating easily in various endocavity regions. The proposed method utilizes transmit array system to generate LP excitation. The magnetic flux created by the resonator depends on the orientation on the LP B_1-field with respect to the resonator. This is the main principle of the applied method here. When the resonator axis is parallel to the applied LP transmit field, only

reception coupling remains and transmission coupling is canceled. Therefore, the improved SNR at the vicinity of the resonator can be explained only with the signal amplification during reception.

In this part, only two ports (x and y) of eight ports of the transmit array system are used to generate LP RF excitation. The amplitudes of the equiphase RF pulses are scaled to steer the generated field. The transmit array system is embedded in the scanner and using only two ports makes it much more accessible and easy to work with. While the transmit array system has been introduced as a commercial product, it is used only for research purposes. The x and y ports of the transmit array system are initially unbalanced. Thus, to obtain LP excitation, the ports have to be adjusted. Fine calibrating the ports results in appropriate reverse polarization. The essence of this method concentrates on homogenizing high-frequency B_1-field and can be proposed as a promising candidate for clinical applications.

Here the SNR and imaging performance of the decoupled resonator in its vicinity are directly related to the reception signal enhancement. Therefore, the resonator characteristics and geometry play an important role on the receive coupling. The LP excitation applied in our experiments has a higher average SAR than the circularly-polarized excitation. While the average SAR build-up by the LP excitation is double of the circular excitation, the circulating excitation creates a smaller peak SAR value compared with the LP excitation because of the asymmetric distribution of the electric field of the LP excitation. Heating test results show that, in the worst-case scenario (when the resonator is coupled with the excitation field), a maximum SAR gain of 1.48 is found around the resonator. Magnetically decoupled device is expected to show a lower SAR gain due to intrinsically decoupled E-field on the resonator. The preliminary phantom and in vivo experiment results indicate that the proposed passive device and excitation technique can provide SNR and resolution enhancement in the vicinity of the interventional device in addition to minimizing the safety hazards.

This work in the thesis demonstrates a localized MR endocavity imaging technique that relies on LP excitation together in conjunction with a passive RF

resonator probe structure. Transmit coupling between RF excitation and passive resonator leads to safety concerns and FA inhomogeneity. Using a linearly driven birdcage coil, the device is decoupled from the LP excitation field, therefore resulting in minimized safety problem and preventing FA inhomogeneity. Transmit decoupling leaves the resonator probe only in reception amplification position; consequently SNR and/or resolution enhancement occur in the vicinity of the resonator without B_1-field distortion. This approach can be extended to variants of such thin-film microwave resonators and other endocavities.

The finding of the thesis show that thin-film microwave resonators are effective tools for wireless sensing and marking. We believe that these wireless devices hold great promise for applications in future health care technologies.

6.1 Contributions to the Literature

6.1.1 Journal Papers

[1]. **A.Alipour**, E.Unal, S.Gokyar, and H.V.Demir. "Development of a distance-independent wireless passive RF resonator sensor and a new telemetric measurement technique for wireless strain monitoring". Sensors and Actuators: Physical A, 255, 87-93, (2017).

[2]. **A.Alipour**,S.Gokyar, O.Algin, E.Atalar, and H.V.Demir. "An Inductively coupled ultra-thin, flexible and passive RF resonator for MRI marking and guiding purposes: clinical feasibility". In submission to MRM.

[3]. **A.Alipour**, V.Acikel, S.Gokyar, O.Algin, C.Oto, E.Atalar, and H.V.Demir. "An inductively receive-only passive resonator probe decoupled using linearly polarized excitation for endocavity MRI imaging". Under submission.

[4]. S.Gokyar, **A.Alipour**, E.Atalar, and H.V.Demir. "Tunable

deep-subwavelength metamaterial enabling sub-mm resolution magnetic resonance imaging". Submitted to Sensors and Actuators: Physical A.

[5]. S.Gokyar, **A.Alipour**, E.Atalar, and H.V.Demir "Magnetic Resonance Imaging of Subdural Electrodes in Brain Assisted by Wireless Implantable Fiducial e-Markers". In submission to IEEE TMI.

6.1.2 Conference Papers

[6]. **A.Alipour**, S.Gokyar, E.Unal, and H.V.Demir "Thin film resonator marker for interventional MRI". MRI-Balkan 2014, Ankara, Turkey.

6.2 Additional Contributions

Also, in the duration of the thesis work, additional contributions include:

6.2.1 Journal Papers

[7]. **A.Alipour**, Z.S.Erdem, V.K.Shamra, M.Utkur, P.Hernandez, E.U.Saritas, and H.V.Demir. "A new class of cubic SPIONs as a dual-mode T_1 and T_2 contrast agent for MRI". Under submission.

[8]. V.K.Shamra, **A.Alipour**, Z.Soran, G.Aykut, and H.V.Demir. "Highly monodisperse low-magnetization magnetite nanocubes as simultaneous $T_1 - T_2$ MRI contrast agents". Nanoscale, 7, 10519-10526, (2015).

[9]. V.K.Shamra, **A.Alipour**, Z.Soran, G.Aykut, and H.V.Demir. "Fluorescent heterodoped nanotetrapods as synergistically enhancing positive and negative

MRI contrast agents". ACS Applied Materials and Interfaces, 8, 12352-12359, (2016).

[10]. S.Fardindoost, **A.Alipour**, S. Mohammadi, S.Gokyar, R.Sarvari, A.Irajizad , and H.V.Demir. "Flexible strain sensors based on electrostatically actuated graphene flakes". Journal of Micromechanics and Microengineering, 25(7), 075016, (2015).

[11]. B.Silemek; **A.Alipour**, V.Acikel, C.Oto, O.Algin, E.Atalar. "A Temperature Sensor Implant for Active Implantable Medical Devices for in vivo Subacute Heating Tests under MRI". In submission to MRM.

6.2.2 Conference Papers

[12]. **A.Alipour**, S.Fardindoost, S. Mohammadi, S.Gokyar, R.Sarvari, A.Irajizad, and H.V.Demir. "Ultrasensitive flexible graphene-based resonator sensor for strain sensing". IEEE RWW 2016, Austin, USA.

[13]. **A.Alipour**, V.K.Shamra, Z.Soran, G.Aykut, and H.V.Demir. "Colloidal nanoparticles for synergistic MRI contrast agent". ISMRM 2016, Singapore.

[14]. **A.Alipour**, V.K.Shamra, Z.Soran, and H.V.Demir "Synthesis of Uniform Iron Oxide Nanoparticles Tuned from Spheres to Cubes". IWMPI 2015, Istanbul, Turkey.

Appendix A

Institutional ethics review board

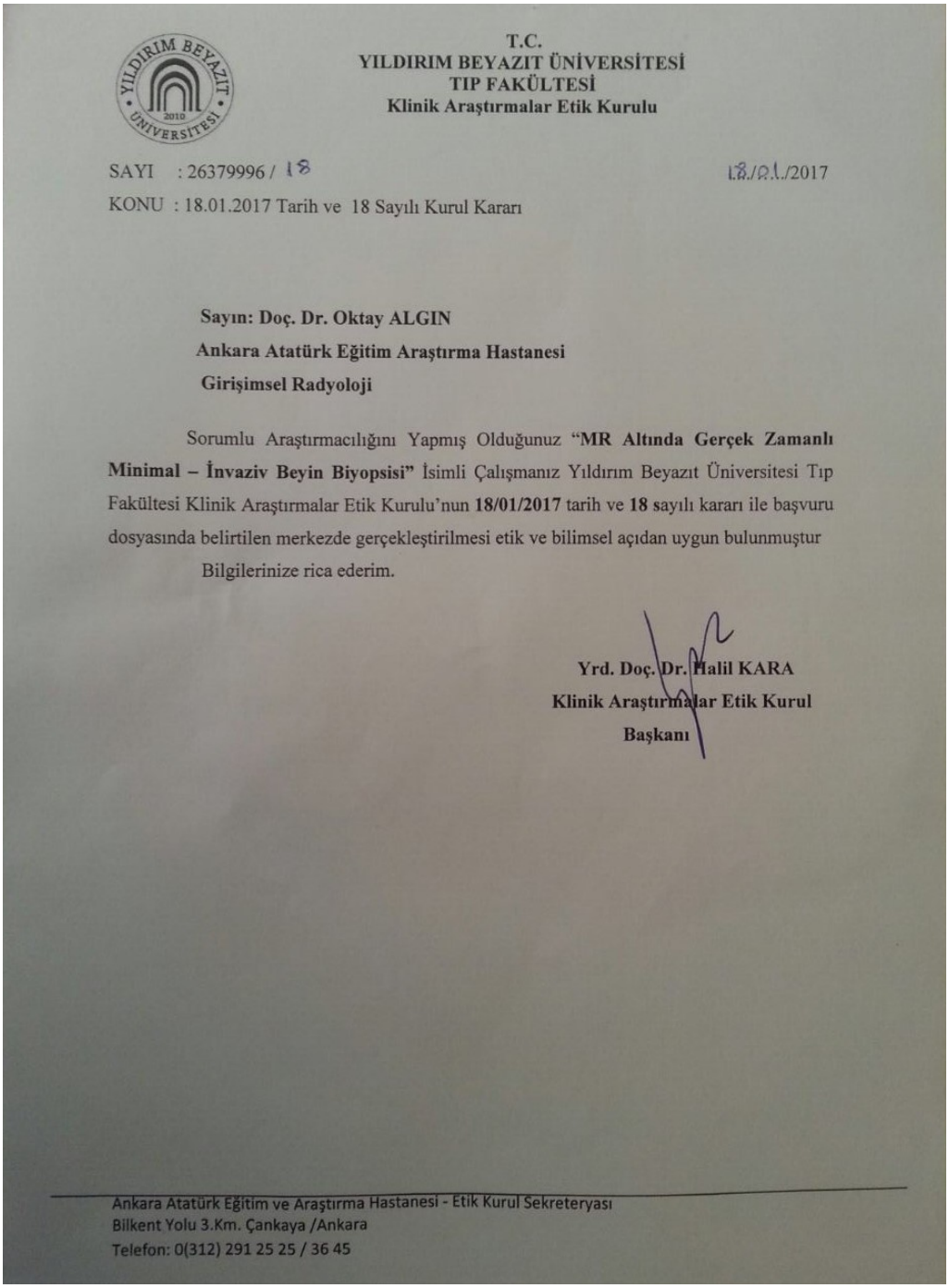

T.C.
YILDIRIM BEYAZIT ÜNİVERSİTESİ
TIP FAKÜLTESİ
Klinik Araştırmalar Etik Kurulu

SAYI : 26379996 / 18 — 18/01/2017

KONU : 18.01.2017 Tarih ve 18 Sayılı Kurul Kararı

Sayın: Doç. Dr. Oktay ALGIN
Ankara Atatürk Eğitim Araştırma Hastanesi
Girişimsel Radyoloji

Sorumlu Araştırmacılığını Yapmış Olduğunuz **"MR Altında Gerçek Zamanlı Minimal – İnvaziv Beyin Biyopsisi"** İsimli Çalışmanız Yıldırım Beyazıt Üniversitesi Tıp Fakültesi Klinik Araştırmalar Etik Kurulu'nun **18/01/2017** tarih ve **18** sayılı kararı ile başvuru dosyasında belirtilen merkezde gerçekleştirilmesi etik ve bilimsel açıdan uygun bulunmuştur

Bilgilerinize rica ederim.

Yrd. Doç. Dr. Halil KARA
Klinik Araştırmalar Etik Kurul
Başkanı

Ankara Atatürk Eğitim ve Araştırma Hastanesi - Etik Kurul Sekreteryası
Bilkent Yolu 3.Km. Çankaya /Ankara
Telefon: 0(312) 291 25 25 / 36 45

Figure A.1: Clinical ethics committee decision

BİLKENT ÜNİVERSİTESİ HAYVAN DENEYLERİ ETİK KURUL KARARI

TOPLANTI TARİH : 30.06.2014
TOPLANTI NO : 4
DOSYA NO : 38
KARAR NO : 2014/38

Bilkent Üniversitesi öğretim üyelerinden Doç.Dr. Hilmi Volkan Demir'in "Manyetik Rezonans Görüntülemesi (MRG) için işaretleyici olarak mikrofabrikasyon ile üretilen ve implant edilebilir yenilikçi esnek rezonatör çipler" başlıklı araştırma deney protokolü Hayvan Deneyleri Etik Kurulu'nda incelenmiş, yapılan inceleme sonucunda çalışmanın Hayvan Deneyleri Etik Kurulu Yönergesi'ne göre uygun bulunarak onaylanmasına katılan üyelerin oy birliği ile karar verilmiştir.

İhsan Gürsel (Başkan)

Ergin Atalar (Üye)

Michelle Adams (Üye)

Z. Gamze Aykut (Üye)

Ahmet Raşit Öztürk (Üye) (katılmadı ve oy kullanmadı)

Teoman König (Üye)

Figure A.2: Animal ethics committee decision

Bibliography

[1] S. D. WB Spillman Jr, "Noncontact power/interrogation system for smart structures," *Smart Structures and Materials*, vol. 2191, pp. 362–372, 1994.

[2] A. Daliri, A. Galehdar, W. S. Rowe, K. Ghorbani, and S. John, "Utilising microstrip patch antenna strain sensors for structural health monitoring," *Journal of Intelligent Material Systems and Structures*, vol. 23, no. 2, pp. 169–182, 2012.

[3] X. Yi, C. Cho, J. Cooper, Y. Wang, M. M. Tentzeris, and R. T. Leon, "Passive wireless antenna sensor for strain and crack sensingelectromagnetic modeling, simulation, and testing," *Smart Materials and Structures*, vol. 22, no. 8, p. 085009, 2013.

[4] S. Weiss, T. Kuehne, F. Brinkert, G. Krombach, M. Katoh, T. Schaeffter, R. W. Guenther, and A. Buecker, "In vivo safe catheter visualization and slice tracking using an optically detunable resonant marker," *Magnetic Resonance in Medicine*, vol. 52, no. 4, pp. 860–868, 2004.

[5] O. Unal, F. R. Korosec, R. Frayne, C. M. Strother, and C. A. Mistretta, "A rapid 2D time-resolved variable-rate k-space sampling MR technique for passive catheter tracking during endovascular procedures.," *Magn Reson Med*, vol. 40, no. 3, pp. 356–362, 1998.

[6] F. Martín, J. Bonache, F. Falcone, M. Sorolla, and R. Marqués, "Split ring resonator-based left-handed coplanar waveguide," *Applied Physics Letters*, vol. 83, no. 22, pp. 4652–4654, 2003.

[7] H. Celik, A. Ulutürk, T. Tali, and E. Atalar, "A catheter tracking method using reverse polarization for MR-guided interventions," *Magnetic Resonance in Medicine*, vol. 58, no. 6, pp. 1224–1231, 2007.

[8] W. R. Overall, J. M. Pauly, P. P. Stang, and G. C. Scott, "Ensuring safety of implanted devices under MRI using reversed RF polarization," *Magnetic Resonance in Medicine*, vol. 64, no. 3, pp. 823–833, 2010.

[9] H. Celik and E. Atalar, "Reverse polarized inductive coupling to transmit and receive radiofrequency coil arrays," *Magnetic Resonance in Medicine*, vol. 67, no. 2, pp. 446–456, 2012.

[10] Y. Eryaman, B. Akin, and E. Atalar, "Reduction of implant RF heating through modification of transmit coil electric field," *Magnetic Resonance in Medicine*, vol. 65, no. 5, pp. 1305–1313, 2011.

[11] Y. Eryaman, E. A. Turk, C. Oto, O. Algin, and E. Atalar, "Reduction of the radiofrequency heating of metallic devices using a dual-drive birdcage coil," *Magnetic Resonance in Medicine*, vol. 69, no. 3, pp. 845–852, 2013.

[12] P. Zhao, N. Deng, X. Li, C. Ren, and Z. Wang, "Development of highly-sensitive and ultra-thin silicon stress sensor chips for wearable biomedical applications," *Sensors and Actuators, A: Physical*, vol. 216, pp. 158–166, 2014.

[13] S. F. Pichorim and P. J. Abatti, "Biotelemetric passive sensor injected within tendon for strain and elasticity measurement," *IEEE Transactions on Biomedical Engineering*, vol. 53, no. 5, pp. 921–925, 2006.

[14] J. C. Butler, A. J. Vigliotti, F. W. Verdi, and S. M. Walsh, "Wireless, passive, resonant-circuit, inductively coupled, inductive strain sensor," *Sensors and Actuators, A: Physical*, vol. 102, no. 1-2, pp. 61–66, 2002.

[15] P. Broutas, H. Contopanagos, E. D. Kyriakis-Bitzaros, D. Tsoukalas, and S. Chatzandroulis, "A low power RF harvester for a smart passive sensor tag with integrated antenna," *Sensors and Actuators, A: Physical*, vol. 176, pp. 34–45, 2012.

[16] Y. Jia, K. Sun, F. J. Agosto, and M. T. Quiñones, "Design and characterization of a passive wireless strain sensor," *Measurement Science and Technology*, vol. 17, no. 11, pp. 2869–2876, 2006.

[17] H. J. Lee and J. G. Yook, "Recent research trends of radio-frequency biosensors for biomolecular detection," 2014.

[18] A. Daliri, A. Galehdar, S. John, C. H. Wang, W. S. T. Rowe, and K. Ghorbani, "Wireless strain measurement using circular microstrip patch antennas," *Sensors and Actuators, A: Physical*, vol. 184, pp. 86–92, 2012.

[19] X. Yi, T. Wu, Y. Wang, R. T. Leon, M. M. Tentzeris, and G. Lantz, "Passive wireless smart-skin sensor using RFID-based folded patch antennas," *International Journal of Smart and Nano Materials*, vol. 2, pp. 22–38, 2011.

[20] R. Melik, E. Unal, N. K. Perkgoz, C. Puttlitz, and H. V. Demir, "Metamaterial-based wireless RF-MEMS strain sensors," in *Proceedings of IEEE Sensors*, pp. 2173–2176, 2010.

[21] R. Melik, "Novel wireless RF-bioMEMS implant sensors of metamaterials," *Ph.D thesis, Department of Electrical and Electronics Engineering, Bilkent University*, 2010.

[22] K. C. McGilvray, E. Unal, K. L. Troyer, B. G. Santoni, R. H. Palmer, J. T. Easley, H. V. Demir, and C. M. Puttlitz, "Implantable microelectromechanical sensors for diagnostic monitoring and post-surgical prediction of bone fracture healing," *Journal of Orthopaedic Research*, vol. 33, no. 10, pp. 1439–1446, 2015.

[23] I. Jones, L. Ricciardi, L. Hall, H. Hansen, V. Varadan, C. Bertram, S. Maddocks, S. Enderling, D. Saint, S. Al-Sarawi, and D. Abbott, "Wireless RF communication in biomedical applications," *Smart Materials and Structures*, vol. 17, no. 1, p. 015050, 2008.

[24] E. A. U. Diego A. Sanz, Costantino Mitrosbaras and F. Segura-Quijano, "Passive resonators for wireless passive sensor readout enhancement," *Appl. Phys. Lett*, vol. 103, no. 13, 2013.

[25] X. Yang and E. Atalar, "Intravascular MR imaging-guided balloon angioplasty with an MR imaging guide wire: feasibility study in rabbits.," *Radiology*, vol. 217, no. 2, pp. 501–6, 2000.

[26] M. Moche, R. Trampel, T. Kahn, and H. Busse, "Navigation concepts for MR image-guided interventions," 2008.

[27] K. Masamune, E. Kobayashi, Y. Masutani, M. Suzuki, T. Dohi, H. Iseki, and K. Takakura, "Development of an MRI???compatible needle insertion manipulator for stereotactic neurosurgery," *Journal of Image Guided Surgery*, vol. 1, no. 4, pp. 242–248, 1995.

[28] C. Parker, A. Damyanovich, T. Haycocks, M. Haider, A. Bayley, and C. Catton, "Magnetic resonance imaging in the radiation treatment planning of localized prostate cancer using intra-prostatic fiducial markers for computed tomography co-registration," *Radiotherapy and Oncology*, vol. 66, no. 2, pp. 217 – 224, 2003.

[29] C. J. Bakker, R. M. Hoogeveen, J. Weber, J. J. van Vaals, M. A. Viergever, and W. P. Mali, "Visualization of dedicated catheters using fast scanning techniques with potential for mr-guided vascular interventions," *Magnetic Resonance in Medicine*, vol. 36, no. 6, pp. 816–820, 1996.

[30] Y. S. Rubin DL, Ratner AV, "Magnetic susceptibility effects and their application in the development of new ferromagnetic catheters for magnetic resonance imaging.," *Invest Radiol*, vol. 25, no. 12, pp. 1325–1332., 1990.

[31] V. D. Koechli, G. C. McKinnon, E. Hofmann, and G. K. von Schulthess, "Vascular interventions guided by ultrafast MR imaging: Evaluation of different materials," *Magnetic Resonance in Medicine*, vol. 31, no. 3, pp. 309–314, 1994.

[32] J. H. Seppenwoolde, M. A. Viergever, and C. J. G. Bakker, "Passive tracking exploiting local signal conservation: The white marker phenomenon," *Magnetic Resonance in Medicine*, vol. 50, no. 4, pp. 784–790, 2003.

[33] H. H. Quick, M. O. Zenge, H. Kuehl, G. Kaiser, S. Aker, S. Massing, S. Bosk, and M. E. Ladd, "Interventional magnetic resonance angiography with no strings attached: Wireless active catheter visualization," *Magnetic Resonance in Medicine*, vol. 53, no. 2, pp. 446–455, 2005.

[34] M. A. Ertürk, A. M. M. El-Sharkawy, and P. A. Bottomley, "Interventional loopless antenna at 7 T," *Magnetic Resonance in Medicine*, vol. 68, no. 3, pp. 980–988, 2012.

[35] M. Etezadi-Amoli, P. Stang, A. Kerr, J. Pauly, and G. Scott, "Interventional device visualization with toroidal transceiver and optically coupled current sensor for radiofrequency safety monitoring," *Magnetic Resonance in Medicine*, vol. 73, no. 3, pp. 1315–1327, 2015.

[36] M. B. Ooi, M. Aksoy, J. MacLaren, R. D. Watkins, and R. Bammer, "Prospective motion correction using inductively coupled wireless RF coils," *Magnetic Resonance in Medicine*, vol. 70, no. 3, pp. 639–647, 2013.

[37] G. Thörmer, N. Garnov, M. Moche, J. Haase, T. Kahn, and H. Busse, "Simultaneous 3D localization of multiple MR-visible markers in fully reconstructed MR images: Proof-of-concept for subsecond position tracking," *Magnetic Resonance Imaging*, vol. 30, no. 3, pp. 371–381, 2012.

[38] O. C. Richardson, O. Bane, M. L. J. Scott, S. F. Tanner, J. C. Waterton, S. P. Sourbron, T. J. Carroll, and D. L. Buckley, "Gadofosveset-based biomarker of tissue albumin concentration: Technical validation in vitro and feasibility in vivo," *Magnetic Resonance in Medicine*, vol. 73, no. 1, pp. 244–253, 2015.

[39] E. Atalar, P. A. Bottomley, O. Ocali, L. C. L. Correia, M. D. Kelemen, J. A. C. Lima, and E. A. Zerhouni, "High resolution intravascular mri and mrs by using a catheter receiver coil," *Magnetic Resonance in Medicine*, vol. 36, no. 4, pp. 596–605, 1996.

[40] O. Ocali and E. Atalar, "Intravascular magnetic resonance imaging using a loopless catheter antenna," *Magnetic Resonance in Medicine*, vol. 37, no. 1, pp. 112–118, 1997.

[41] S. Fandrey, S. Weiss, and J. M??ller, "A novel active MR probe using a miniaturized optical link for a 1.5-T MRI scanner," *Magnetic Resonance in Medicine*, vol. 67, no. 1, pp. 148–155, 2012.

[42] W. R. Nitz, A. Oppelt, W. Renz, C. Manke, M. Lenhart, and J. Link, "On the heating of linear conductive structures as guide wires and catheters in interventional MRI," *Journal of Magnetic Resonance Imaging*, vol. 13, no. 1, pp. 105–114, 2001.

[43] M. Burl, G. a. Coutts, and I. R. Young, "Tuned fiducial markers to identify body locations with minimal perturbation of tissue magnetization.," *Magnetic resonance in medicine : official journal of the Society of Magnetic Resonance in Medicine / Society of Magnetic Resonance in Medicine*, vol. 36, pp. 491–493, 1996.

[44] H. H. Quick, M. E. Ladd, D. Nanz, K. P. Mikolajczyk, and J. F. Debatin, "Vascular stents as RF antennas for intravascular MR guidance and imaging," *Magnetic Resonance in Medicine*, vol. 42, no. 4, pp. 738–745, 1999.

[45] S. Gokyar, "Novel implantable distributively loaded flexible resonators for MRI," *Master's thesis, Department of Electrical and Electronics Engineering, Bilkent University*, 2011; S.Gokyar, "Novel distributively loaded flexible sub-cm resonators for MRI: from theory to medical," *Ph.D thesis, Department of Electrical and Electronics Engineering, Bilkent University*, in submission.

[46] N. J. Farcich, J. Salonen, and P. M. Asbeck, "Single-length method used to determine the dielectric constant of polydimethylsiloxane," in *IEEE Transactions on Microwave Theory and Techniques*, vol. 56, pp. 2963–2971, 2008.

[47] M. Woytasik, J. P. Grandchamp, E. Dufour-Gergam, J. P. Gilles, S. Megherbi, E. Martincic, H. Mathias, and P. Crozat, "Two- and three-dimensional microcoil fabrication process for three-axis magnetic sensors on flexible substrates," *Sensors and Actuators, A: Physical*, vol. 132, no. 1 SPEC. ISS., pp. 2–7, 2006.

[48] J. P. Hornak, J. Szumowski, and R. G. Bryant, "Magnetic field mapping.," *Magnetic resonance in medicine : official journal of the Society of Magnetic Resonance in Medicine / Society of Magnetic Resonance in Medicine*, vol. 6, pp. 158–163, 1988.

[49] V. Acikel and E. Atalar, "Modeling of radio-frequency induced currents on lead wires during MR imaging using a modified transmission line method," *Medical Physics*, vol. 38, no. 12, pp. 6623–6632, 2011.

[50] T. Nakayoshi, H. Tajiri, K. Matsuda, M. Kaise, M. Ikegami, and H. Sasaki, "Magnifying endoscopy combined with narrow band imaging system for early gastric cancer: Correlation of vascular pattern with histopathology," *Endoscopy*, vol. 36, no. 12, pp. 1080–1084, 2004.

[51] D. Stamper, N. J. Weissman, and M. Brezinski, "Plaque Characterization With Optical Coherence Tomography," 2006.

[52] S. E. Nissen and P. Yock, "Intravascular ultrasound: novel pathophysiological insights and current clinical applications.," *Circulation*, vol. 103, no. 4, pp. 604–616, 2001.

[53] G. W. Falk, "Autofluorescence Endoscopy," 2009.

[54] R. Cardoso, N. Coburn, R. Seevaratnam, R. Sutradhar, L. G. Lourenco, A. Mahar, C. Law, E. Yong, and J. Tinmouth, "A systematic review and meta-analysis of the utility of EUS for preoperative staging for gastric cancer," 2012.

[55] J. a. Schaar, F. Mastik, E. Regar, C. a. den Uil, F. J. Gijsen, J. J. Wentzel, P. W. Serruys, and a. F. W. van der Stehen, "Current diagnostic modalities for vulnerable plaque detection.," *Current pharmaceutical design*, vol. 13, no. 10, pp. 995–1001, 2007.

[56] K. J. Kang KJ, Kim KM, Min BH, Lee JH, "Endoscopic Submucosal Dissection of Early Gastric Cancer," *Gut Liver*, vol. 5, no. 4, pp. 418–426, 2011.

[57] G. Angelelli, A. A. S. Ianora, A. Scardapane, P. Pedote, M. Memeo, and A. Rotondo, "Role of computerized tomography in the staging of gastrointestinal neoplasms," 2001.

[58] K. T. Takashima S, Takeuchi N, Shiozaki H, Kobayashi K, Morimoto S, Ikezoe J, Tomiyama N, Harada K, Shogen K, "Carcinoma of the esophagus: CT vs MR imaging in determining resectability," *AJR Am J Roentgenol*, vol. 156, no. 2, pp. 297–302., 1991.

[59] D. J. Gilderdale, A. D. Williams, U. Dave, and N. M. DeSouza, "An inductively-coupled, detachable receiver coil system for use with magnetic resonance compatible endoscopes," *Journal of Magnetic Resonance Imaging*, vol. 18, no. 1, pp. 131–135, 2003.

[60] S. Sathyanarayana and P. a. Bottomley, "MRI endoscopy using intrinsically localized probes," *Medical Physics*, vol. 36, no. 3, p. 908, 2009.

[61] R. M. Syms RR, Young IR, Ahmad MM, Taylor-Robinson SD, "Design of Magneto-Inductive Magnetic Resonance Imaging Catheters," *IEEE Trans Biomed Eng*, vol. 60, no. 9, pp. 2421–2431, 2013.

[62] O. B. J.-M. Verret, F. Pilleul, C. Rabrait, E. Malher, S. Piranda, J-F. Delforge, H. Saint-James, "Characterization of a dedicated double loop, endoluminal coil for anal sphincter MR imaging at 1.5 T and 3 T," *Concepts Magn. Reson*, vol. 44, pp. 39–49, 2014.

[63] S. Zuehlsdorff, R. Umathum, S. Volz, P. Hallscheidt, C. Fink, W. Semmler, and M. Bock, "MR coil design for simultaneous tip tracking and curvature delineation of a catheter," *Magnetic Resonance in Medicine*, vol. 52, no. 1, pp. 214–218, 2004.

[64] A. K. Homagk, R. Umathum, M. Korn, M. A. Weber, P. Hallscheidt, W. Semmler, and M. Bock, "An expandable catheter loop coil for intravascular MRI in larger blood vessels," *Magnetic Resonance in Medicine*, vol. 63, no. 2, pp. 517–523, 2010.

[65] D. S. Rivera, M. S. Cohen, W. G. Clark, A. C. Chu, R. L. Nunnally, J. Smith, D. Mills, and J. W. Judy, "An implantable RF solenoid for magnetic resonance microscopy and microspectroscopy," *IEEE Transactions on Biomedical Engineering*, vol. 59, no. 8, pp. 2118–2125, 2012.

[66] Y. I. Segkhoonthod K, Syms RR, "Design of Magneto-Inductive Magnetic Resonance Imaging Catheters," *IEEE Sensors Journal*, vol. 14, no. 15, pp. 1505–1513, 2014.

[67] W. Wang, C. L. Dumoulin, A. N. Viswanathan, Z. T. H. Tse, A. Mehrtash, W. Loew, I. Norton, J. Tokuda, R. T. Seethamraju, T. Kapur, A. L. Damato, R. A. Cormack, and E. J. Schmidt, "Real-time active MR-tracking of metallic stylets in MR-guided radiation therapy," *Magnetic Resonance in Medicine*, vol. 73, no. 5, pp. 1803–1811, 2015.

[68] C. D. Constantinides, E. Atalar, and E. R. McVeigh, "Signal-to-noise measurements in magnitude images from NMR phased arrays," *Magnetic Resonance in Medicine*, vol. 38, no. 5, pp. 852–857, 1997.